Strata structure interpretation and mud volcanism activity analysis at the Zhurong landing site

Xiaojian Xu[1,2,3], Zhizhong Kang[1,2,3*], Yu Yang[1,2,3], Teng Hu[1,2,3], Dong Wang[4] Xing Du[1,2,3], Juan Xie[1,2,3], Yehua Ma[1,2,3]

[1]School of Land Science and Technology, China University of Geosciences (Beijing), Beijing, China; [2]Research Center of Lunar and Planetary Remote Sensing Exploration, China University of Geosciences (Beijing), Beijing, China; [3]Subcenter of International Cooperation and Research on Lunar and Planetary Exploration, Center of Space Exploration, Ministry of Education of the People's Republic of China, Beijing, China; [4]Changchun Institute of Optics, Fine Mechanics and Physics, Chinese Academy of Sciences, Changchun, China

Corresponding author: Zhizhong Kang (zzkang@cugb.edu.cn)

Key points

- 3D strata model suggests that volume compaction coincides with underground material ejection during the formation of partial ghost craters.
- The cones at Zhurong landing site are mud volcanoes, and the underground magma chamber in the south is the heat source for their formation.
- After VBF formed at 3.43Ga, water evaporation, underground thermal activity and meteorite impacts caused the landform at Zhurong landing site.

Abstract

China's first Mars Exploration Mission Tianwen-1 achieved full success. The loaded Zhurong Rover landed south of the Utopia Planitia. The Tianwen-1 orbiter also sends back high-resolution images. We utilized the High-Resolution Imaging Camera (HiRIC) of Tianwen-1 and Context Camera (CTX) loaded on the Mars Reconnaissance Orbiter (MRO) to collect the image data and construct a 3D strata model of the Zhurong landing site. Using this model, we analyzed the material loss of ghost craters. Judging from the morphological and spectral characteristics of pitted cones at the Zhurong landing site, we confirmed their classification as mud volcanoes and rootless cones. We also analyzed the possible cause of formation by combining the gravity field and magnetic field data. The experimental results indicate that (1) the Zhurong landing site can be divided into the dry sedimentary, moisture sedimentary, and Vastitas Borealis (VB) members as three strata and another ejecta blocks. The three strata are categorized into VB formations with an integral width of 1.2 km. (2) The cones at the Zhurong landing site are mud volcanoes and rootless cones formed by groundwater activity. The heat source originates from a southern underground magma chamber. The density of mud volcanoes signifies the existence of ejecta blocks.

(3) Apart from volumetric compaction, some ghost craters show the eruption of underground substances. Generally, after the VB unit located on the surface of the Zhurong landing site surface formed 3.43Ga, the current geomorphology of the landing site was altered due to interior and exterior geological activities, such as the differentiation of water evaporation above ground and underground, underground thermal activity, and meteorite impacts.

Plain Language Summary

The water environment and its evolution history on Mars is one of the important research topics of planetary science. Zhurong Rover of Tianwen-1 Mission landed in the south of Utopia Planitia and provides the latest data for the investigation on this topic. By taking advantage of these high-resolution images combined with collected data from past Mars Exploration Missions, we constructed a 3D strata model at the Zhurong landing site to confirm the three-layered structure and ejecta blocks at the site. Through morphological analysis, we determined that the cones at the site are very likely mud volcanoes and discovered the thermal power source formed by combining gravity fields and magnetic data. Our research shows that the Zhurong landing site covers 1.2 km thick paleomarine sediments. After the disappearance of surface water at the site approximately 3.43 Ga ago, effects including water evaporation differences above ground and underground, underground thermal activity and meteorite collision characterize the formation of geographical morphology at the site.

1. Introduction

Zhurong Rover, China's first Mars rover equipped with the Tianwen-1 (TW-1) lander, successfully landed at the target site in southern Utopia Planitia on 15th May 2021. TW-1 Mission plans to achieve orbiting, landing and roving on Mars to carry out globally and synthetically orbital survey and regionally patrol exploration in a launch (Wang et al., 2020). Thus, the TW-1 detector consists of an orbiter and lander, and the lander contains an entry capsule and rover. There are five scientific objectives in the TW-1 Mission: (1) Mars morphology and geological structure characteristics; (2) Soil characteristics and water/ice distribution on the surface; (3) Material composition on the surface; (4) Atmospheric ionosphere, surface climate and environmental characteristics; and (5) Physical field and internal structure. Based on these objectives, southern Utopia Planitia was chosen as the landing site (Wang et al., 2020). At present, the Zhurong Rover is traveling to the ancient coast to the south to implement the expansion task. The investigation by the Zhurong Rover and TW-1 orbiter can help researchers study the evolution of the paleo-ocean environment and the features of water/ice activities in the southern Utopia Planitia.

Through the statistical analysis of 10–55° N, 210–260° W cones in the Utopia Planitia, Depablo et al. (2009) believe that the formation of cones in this area is related to mega lahars, debris flows and outflows in Elysium Province and

the Utopia Planitia. Soare et al. (2005, 2013, 2020) conducted continuous research that lasted over a decade. The morphologies, scale, height and surface textures of the cones on the Utopia Planitia are consistent with Tuktoyaktuk Coastlands in northern Canada, closed-system ice core pingos in north-central Alaska and northeast Russia on Earth. Ye at al. (2021) measured 130 cones in Zhurong landing site using context imager (CTX) digital elevation models (DEMs). Combining high resolution imaging science experiment (HiRISE) data they supported the mud volcano origin hypothesis of the cones. Because, mud volcanoes are an important source of methane release into the atmosphere on Earth, cones are not only invaluable windows into the subsurface, but also intriguing astrobiology targets for Martian life. Huang et al. (2021) identified 272 cones in Zhurong landing area using High-Resolution Imaging Camera (HiRIC) images collected by the TW-1 orbiter. They derived the skewness-kurtosis relationship of Martian mud volcanoes and interpreting the cones in the landing area as mud volcanoes. Therefore, the cones on the Utopia Planitia are not only evidence showing the former existence of liquid water on the Mars surface but also marks of freeze-thaw cycling of the Amazonian ice layer. Ivanov et al. (2014) utilized high-resolution images covering approximately 80-85% of the selected region in the Utopia Planitia to conduct detailed mapping and discover the mud volcanism landforms represented by etched flows. Therefore, it is considered that there are a large number of water bodies in the middle of the Utopia Planitia. Recently, Mangold et al. (2021) employed the returned data of the perseverance rover and the presence of strata discovered at the western edge of Jezero crater by HiRSE imaging. They further analyzed and discovered that intermittent floods occurred in the region, and explored ancient lakes that may have transitioned from sustained hydrologic activity in a persistent lake environment to highly energetic short-duration fluvial flows. For Tianwen-1's landing site, Wu et al. (2021) utilized multiple sourced Mars Reconnaissance Orbiter (MRO) data and the Mars Global Surveyor (MGS) to conduct a geographical investigation of the thermophysical properties, landform features, and substance compositions of the region to highlight what the Tianwen-1 Mission has determined as critical information for the study of water environment evolution in the region. It is noteworthy that the current research results mainly involve the interpretation of surface morphology. If the spatial structure distribution of strata can be further interpreted by remote sensing technology, it will contribute to the interpretation of the regional geological evolution history.

A number of researchers has been investigated the presence of a layered stratigraphy in planetary crusts revealed by fresh craters. Some laboratory experiments pointed out that an increase in the target material strength with depth caused the modification of simple craters into central-mound, flat bottom, and concentric (Oberbeck & Quaide, 1967; Ormö et al., 2013). Senft and Stewart (2007), presented the results for cratering into idealized terrains with layers of differing material strength and pointed out that as long as there is a sufficient difference in strength between the regolith and the underlying surface, the same morphological progression of crater morphology will be achieved. Then they showed

that the presence of an icy layer could modify the crater mechanics and produce changes in the final shape of the craters (Senft & Stewart, 2008). Herrick and Hynek (2017) also suggested that some flat floors might develop in martain craters for the presence of a hard layer which underneath a weak layer, but others represent that floor is covered by later sediments that obscure the original structures. Systematic numerical simulations carried out by Prieur et al. (2018) show that the crater morphology is affected by impact velocity and the material strength of the target. Martellato et al. (2020) select two simple craters with concentric morphology and numerically model their formation to investigate the dependence of the final crater morphology on the material model parameters.

This paper measures the depth of flat-bottomed craters on DEM producted by high-resolution images to construct a 3D strata model of the Zhurong landing site and accomplish the interpretation of strata. By analyzing and estimating the water ice layer buried depth in the crater, the team determined the spatial distribution of the water-containing ice layer. The team further utilized multiple source data of gravity and magnetic fields to interpret the strata structure in the landing site to explore the mud volcano formation reason and scale at the Zhurong landing site to facilitate water thermal activity and evolutionary history studies at the Zhurong landing site.

2. Study Area and Data

2.1 Study Area

At 7:18 on May 15, 2021, the Tianwen-1 Landing Patrol - Zhurong Rover completed a successful landing. The landing site located at 109.92°E, 25.06°S is the junction of ancient land and ocean at the southern end of the Utopia Planitia in the northern hemisphere of Mars.

Utopia Planitia is the largest plane on Mars with a diameter of 3200 km. Its center is located at 49.7°N, 118°E and was formed during the Noachian (McGill, 1989). The southern region of the Utopian Planitia is flat with a lack of large meteorite craters or gullies. The terrain around the Utopian basin is complex. The edge of the basin is the crustal dichotomy boundary in the south and west of Mars, the southwest is adjacent to Isidis Planitia, the east is adjacent to Elysium Province, and an unnamed arcuate ridge acts as the dividing line between the north polar and the Utopian basin (Thomson, 2001). The geomorphic characteristics of Utopia Planitia show that this area may be an ancient ocean, which is closely related to the evolution of the Martian water environment, making it an important area in Martian exploration (Ivanov, 2014). There are many special geomorphic units in the southern Utopian Planitia, such as rampart craters, pancake-like ejecta craters, ghost craters, mesas, dunes, etc. (Mills, 2021). These special geomorphic structures show that the region once had water ice and experienced more intense volcanic activity and wind sand erosion. This area contains a substance called Vastitas Borealis, abbreviated as VB. The VB is a Late Hesperian geomorphic unit, covering most of the northern lowlands of

Mars (Tanaka, 1987). Kreslavsky et al. (Kreslavsky, 2002) believe that this material is composed of marine sediments formed by floods released from outflow channels. The possibility of such an ocean is important because it is related to the potential habitability of ancient Mars.

2.2 Data

All the data in the paper include CTX mosaic images (5 m/pixel resolution, Dickson, 2018) produced by the Malin Space Science Systems and Jet Propulsion Laboratory and panchromatic images (0.7 m/pixel) of the Tianwen-1 HiRIC; HiRIC is one of the main payloads of China's first Mars Exploration Mission. Its main goal is to obtain detailed observation images of key areas on the surface of Mars. It has two working modes: panchromatic mode and multispectral mode (Meng, 2021). The comparison of key parameters between HiRIC and MRO equipped with HiRISE and CTX is shown in Table 1 (Meng, 2021; McEwen, 2007; Malin, 2007). Both HiRIC and HiRISE can provide high-resolution images to characterize the strata, geological structure and composition of Martian surface features in detail (McEwen, 2007); CTX is designed to provide background data obtained by other instruments (Malin, 2007). After comprehensively evaluating the performance parameters and research area of the above three instruments, we selected HiRIC panchromatic images and CTX images. The high-resolution images and DEM offered by HiRIC provide clear morphological features of large areas in the southern Utopia Planitia, which can also accomplish mud volcano statistics and land block division that could not be completed originally due to the small coverage area of HiRISE (Figure 1(a), red is the coverage area of the HiRIC image, yellow is the coverage area of the HiRISE image) and insufficient CTX resolution (Figure 1 (b, c)) It has provided great help for the regional research.

HiRIC DEM (3.5 m/pixel), CTX DEM (8 m/pixel) and MEX HRSC MOLA blended DEM (200 m/pixel, Fergason, 2018) produced by stereophotogrammetry. The HiRIC DEM is used for stratigraphic surveys and block division, the CTX DEM is used for stratigraphic surveys, and the MEX HRSC MOLA blended DEM is used for the analysis of large-scale geomorphic units.

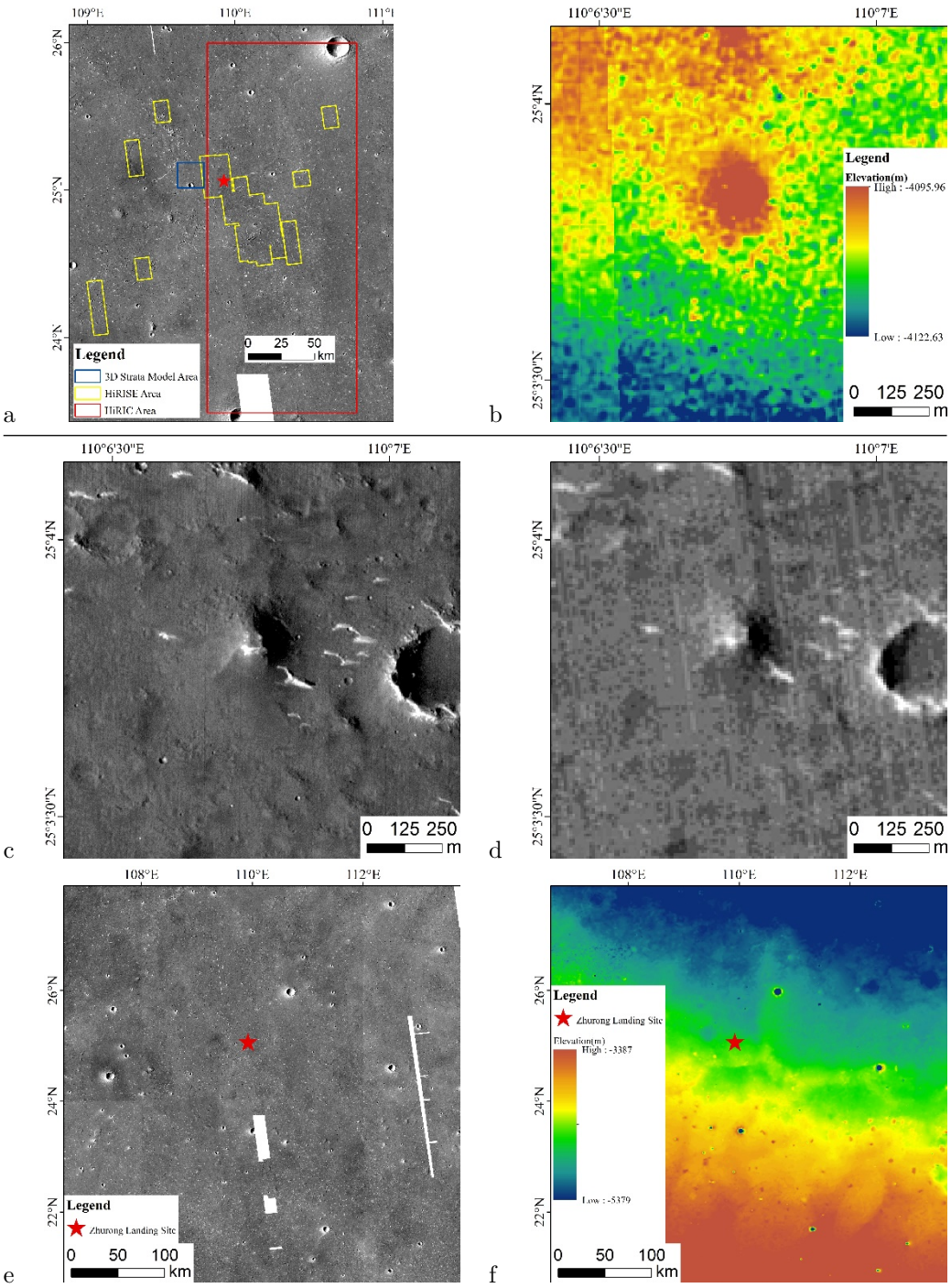
a
109°E
110°E
111°E
26°N
25°N
24°N
Legend
3D Strata Model Area
HiRISE Area
HiRIC Area
0 25 50
km
b
110°6'30"E
110°7'E
25°4'N
25°3'30"N
Legend
Elevation(m)
High : -4095.96
Low : -4122.63
0 125 250
m
c
110°6'30"E
110°7'E
25°4'N
25°3'30"N
0 125 250
m
d
110°6'30"E
110°7'E
25°4'N
25°3'30"N
0 125 250
m
e
108°E
110°E
112°E
26°N
24°N
22°N
Legend
Zhurong Landing Site
0 50 100
km
f
108°E
110°E
112°E
26°N
24°N
22°N
Legend
Zhurong Landing Site
Elevation(m)
High : -3387
Low : -5379
0 50 100
km

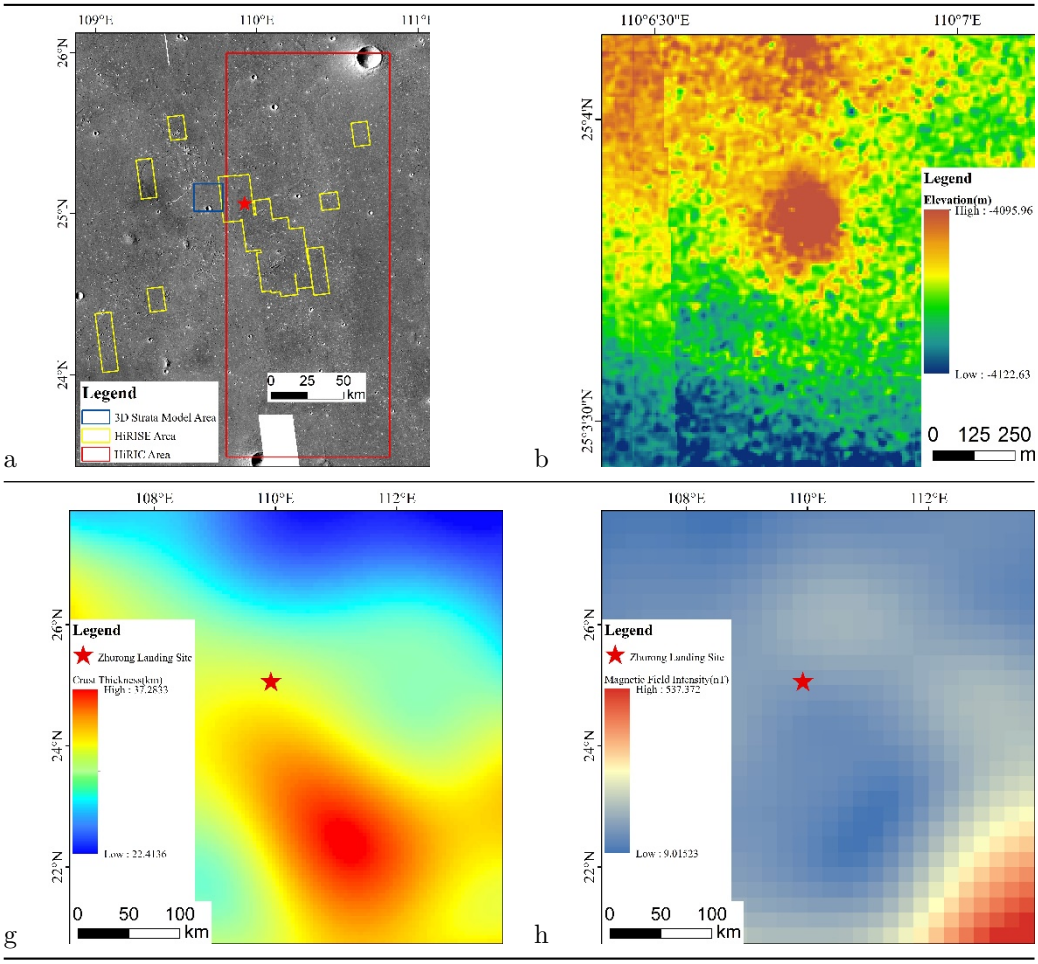

Figure 1 (a) Blue: 3D strata model range, red: HiRIC image coverage, yellow: HiRISE coverage (CTX mosaic ID: E108_N20, E108_N24); (b) Cone on HiRIC DEM; (c) Cone on HiRIC image; (d) Cone on CTX image (CTX mosaic ID: E108_N24); (e) CTX images produced by Malin Space Science System and Jet Propulsion Laboratory in the landing site of Zhurong(CTX mosaic ID: E104_N20, E104_N24, E108_N20, E108_N24, E112_N20, E112_N24); (f) MEX HRSC MOLA Blended DEM in the landing site of Zhurong; (g) Crustal thickness map of Zhurong landing site; (h) Magnetic field intensity diagram of Zhurong landing site;.

The Compact Reconnaissance Imaging Spectrometer for Mars (CRISM) is a VNIR imaging spectrometer operating over the wavelength range: 0.36–3.92 m (Murchie et al., 2007). CRISM has separate S (0.4–1.0 m) and L (1.0–3.9 m) detectors, with a spectral sampling of 6.55 nm/channel (Murchie et al., 2007). The CRISM products we used for cones VNIR spectroscopy analysis are full

resolution targeted (FRT; 18 m/pixel) and multispectral survey mapping (MSV; 200m/pixel). The Mars Mineralogical Spectrometer (MMS) on the Tianwen-1 Mission is also a VNIR imaging spectrometer. It operates over 0.45~1.05 m (V-NIR) and 1~3.4 m (N-NIR), with a spectral sampling of 2.73nm/band (V-NIR) and 7.50nm/band (N-NIR) and resolution is about 280m/pixel (He et al., 2021).

Crustal thickness data (Goossens et al. (2017)). Goossens et al. (2017) calculated the Martian crust thickness based on the NASA GMM-3 gravity model and MOLA topography. A standard density value model of 2900 kg/m^3 is adopted for the crust, and 3500 kg/m^3 is adopted for the mantle.

Mars magnetic field model (160 km/pixel) (Langlais et al. (2019)). Langlais et al. (2019) used MGS magnetometer, electron reflectometer and MAVEN (Mars Atmosphere and Volatile Evolution) magnetometer data to reflect the magnetic field on a sphere with a radius of 3393.5 km. Gravity and magnetic field observations are used to find possible traces of underground tectonic movement.

Table 1 Comparison of parameters among HiRIC CTX and HiRISE

Data	Design resolutions	Height of designed rail	Focal length	Aperture	Sideview	Wave segment	CCD dimension	CCD quantity
HiRIC	Panchromatic 0.5/pixel, Multispectral 2/pixel	km	mm	f/12	°, 9 km	Panchromatic 450 nm 900 nm Multispectral 450 nm 520 nm, 520 nm 600 nm, 520 nm 600 nm, 760 nm 900 nm	μm	
CTX	m/pixel	km	mm	f/3.25	°, 30 km	~700 nm	μm	

Data	Design resolutions	Height of designed rail	Focal length	Aperture	Sideview	Wave segment	CCD dimension	CCD quantity
HiRISE	m/pixel, km	mm	f/24	Red 1.14°, 6 km Color 0.23°, 1.2 km	Red 570~830 nm Turquoise <580 nm Near infrared >790 nm			Red 20048 Colored 4048

3. Method

The research roadmap of this paper is shown in Figure 2. The stratigraphic structure and surface ejecta distribution of the Zhurong landing site are obtained by using the CTX and HiRIC DEM combined with morphological methods. On this basis, the three-dimensional strata model and ejecta block distribution map are made. The three-dimensional strata model is used for the analysis of strata and ghost craters. HiRIC images, MMS and CRISM spectral data are used to study the characters of cone, confirm some of the cones are mud volcanoes. Then, based on the distribution map of the ejecta block, we combined gravity and magnetic data to analyzes the genesis of mud volcanoes and finally analyzes the regional geological evolution characteristics and dynamic mechanism after the formation of the VB.

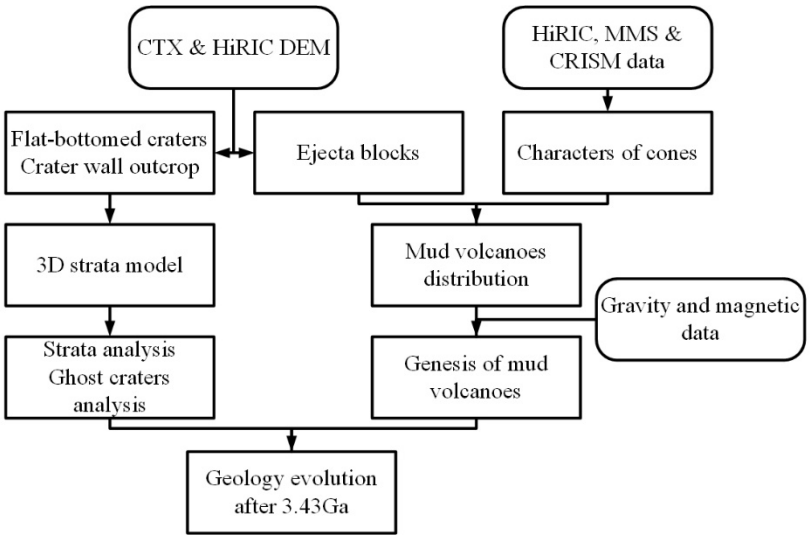

Figure 2 The process of experimental methods

3.1 Morphological method

The surface morphology of Mars is diverse. There are rampart craters (Figure 3(a)), pancake-like ejecta craters (Figure 3(b)), ghost craters (Figure 3(c)), mesas (Figure 3(d)), dunes (Figure 3I), cones (Figure 3(f)) and so on in the south of Utopia Planitia. These unique landforms are the yields of flowing water (Figure 3(a-c)), glacier (Figure 3(d)) or atmospheric action (Figure 3I), which can reflect the paleogeographic environment and evolution history. The special shape of craters can be used as evidence of stratigraphic correlation, assist in the construction of a three-dimensional strata model and indicate the spatial distribution of water bearing strata. Statistics of the spatial distribution characteristics of special landforms, combined with topographic changes, can quantitatively describe the regional characteristics for the division and evolution analysis of different plots.

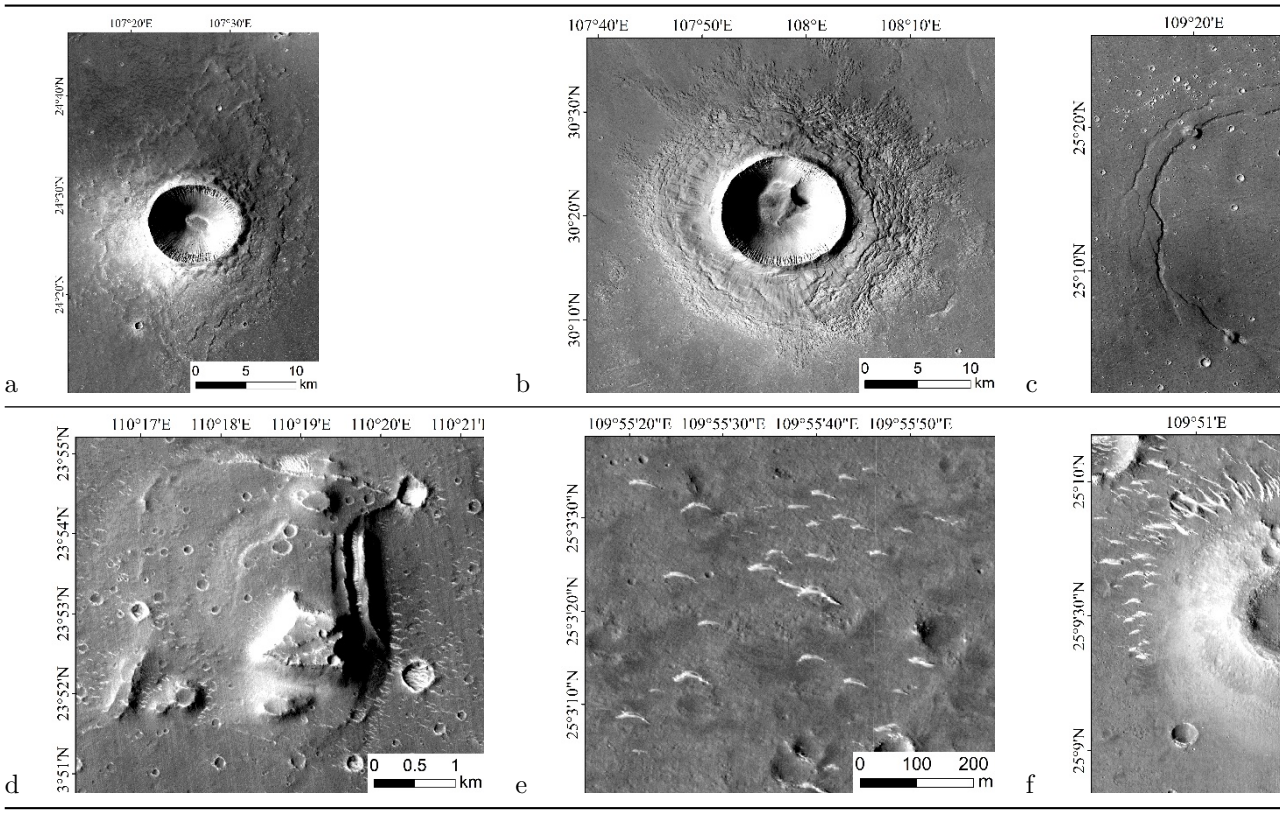

Figure 3 (a) Rampart crater(CTX mosaic ID: E104_N24), (b) pancake-like ejecta crater(CTX mosaic ID: E104_N28, E108_N28), (c) ghost crater(CTX

mosaic ID: E108_N24), (d) mesas, (e) dune, (f) cone.

The rampart crater reflects the distribution of underground water ice (Barlow, 2006), and the burial depth of underground water ice can be estimated by measuring its depth (Niu, 2021). Ghost craters can also be used to study sediment thickness. Some ghost craters have two concentric circular grabens. The thickness of the filler can be estimated by measuring the diameter of rampart craters and the distance of concentric grabens (Mills, 2021). The genesis of the cone is still controversial, mainly including mud volcano, cinder and rootless cone hypotheses (Dapremont, 2021). Various hypotheses have specific genesis and formation environments. Determining the genesis of the cone through morphological characteristics can determine the geological environment of the Zhurong landing site during the formation of the cone.

The study of Herrick and Hynek (2017), Martellato et al. (2020) suggested that the flat floors might develop in craters for the presence of a harder substratum placed at the base of the initial transient cavity, but others represent that floor is covered by sediments such as crater A (Figure 4(a)), a significant fraction is flat-floored due to postimpact deposition or erosion, (Herrick & Hynek, 2017). However flat bottom craters B and C at the Zhurong landing site (Figure 4(b), (c)) are different from those flat-floored due to postimpact deposition or erosion. Considering their diameter, cater A and B are located in the transition section of simple and complex craters. The depth/diameter ratio (d/D) of cater B (0.14) is consistent with typical simple craters, ranging from 0.14 to 0.20 (Herrick & Hynek, 2017). However, the d/D of crater A is only 0.08, obviously lower than the 0.09 d/D value of central pit craters (Herrick & Hynek, 2017), suggests it belongs to a transitional crater whose floor is completely covered by debris slumped from the crater walls (Plescia, 2015) and cannot be used to measure strata. What's more, both crater B and C correspond with the depth/diameter relationships estimated by Robbins and Hynek (2012) (Table 2). The high consistency between them indicates that crater B and C are fresh craters that are not filled and can prove the presence of a harder substratum below. Thus, small flat craters which fit the depth/diameter relationships will be considered fresh enough to be used for measuring strata. The concentric crater shown by Figure 4(d) also suggests the presence of a hard layer which underneath a weak layer which causes the flat bottom structure.

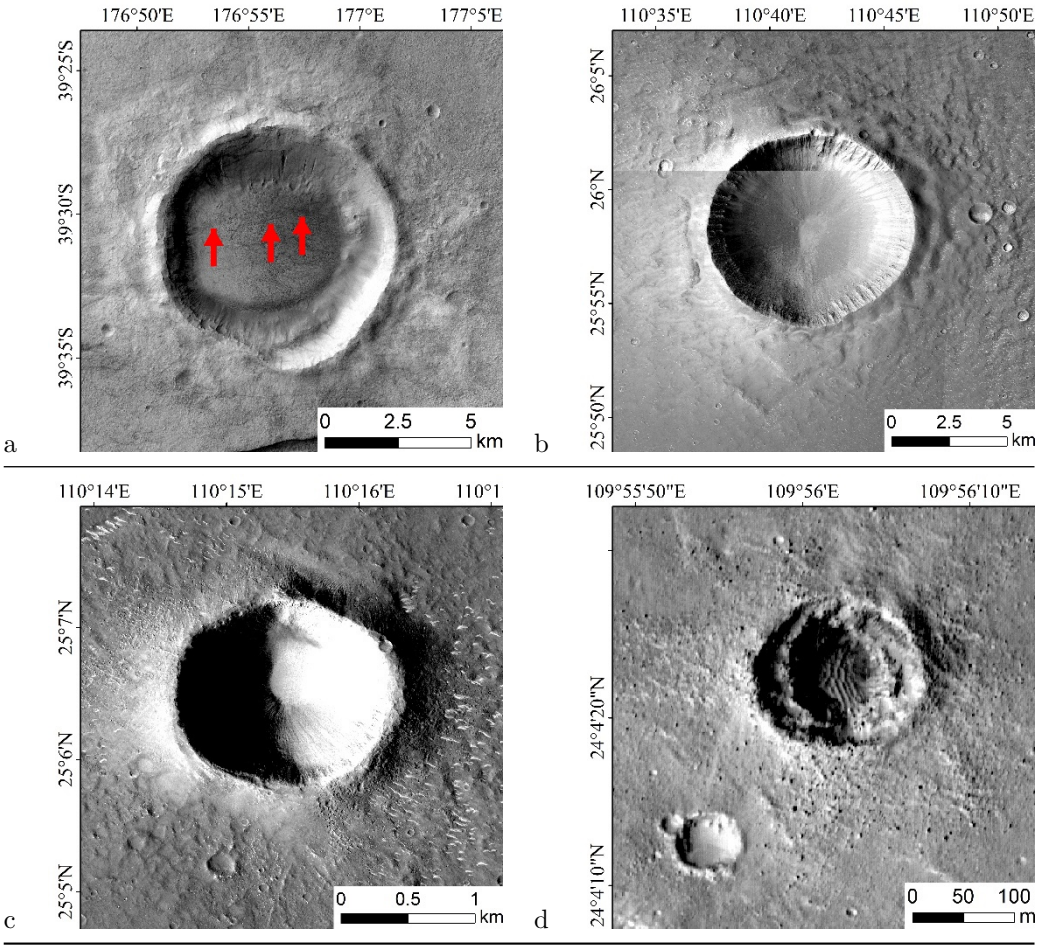

Figure 4 (a) Crater A: A complex flat crater due to postimpact deposition, red arrow: postimpact deposition or erosion (Diameter=8.35km, Depth= 0.7km, CTX mosaic ID: E176_N-40), (b) Crater B: A simple fresh crater in Zhurong landing site (Diameter=9.02km, Depth= 1.28km), (c) Crater C: A simple fresh crater in Zhurong landing site (Diameter=1.64km, Depth= 0.28km), (d) A concentric crater in Zhurong landing site.

Table 2 Crater Depth and Depth/Diameter Relationships (Robbins & Hynek,2012)

Crater	Diameter/km	Depth/km	Estimated Depth/km
B	9.02	1.28	1.29
C	1.64	0.28	0.29

3.2 Measurement of stratigraphic structure and generation of the 3D strata model

When the meteorite energy is high, it will penetrate one or more strata in the process of impact with the planet's surface, making the crater a natural outcrop. Due to the different compositions and mechanical properties of different strata, the crater presents special forms, such as flat bottoms and concentric circles. Therefore, the stratum structure can be measured based on the morphological characteristics of the stratum exposed in the crater (Wilcox, 2005). In Figure 5(a), the depth of the exposed stratum can be obtained by measuring the flat bottom marked by the green ring through the DEM. In addition, each stratum exposed on the impact pit wall may also show different textures and material compositions. The stratum can be identified by high-resolution or spectral images (Figure 5(b)). The weathering of the planetary surface will lead to the degradation of the crater, making it difficult to identify the formation characteristics. The sand and dust on Mars will also fill the interior of the crater, and the strata thickness cannot be measured accurately (Figure 5(c)). Therefore, when measuring the formation depth, it is necessary to select a fresh impact pit to eliminate the error.

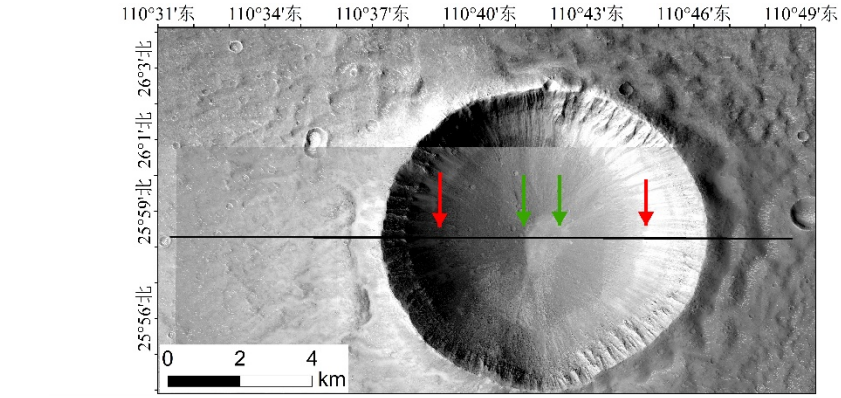

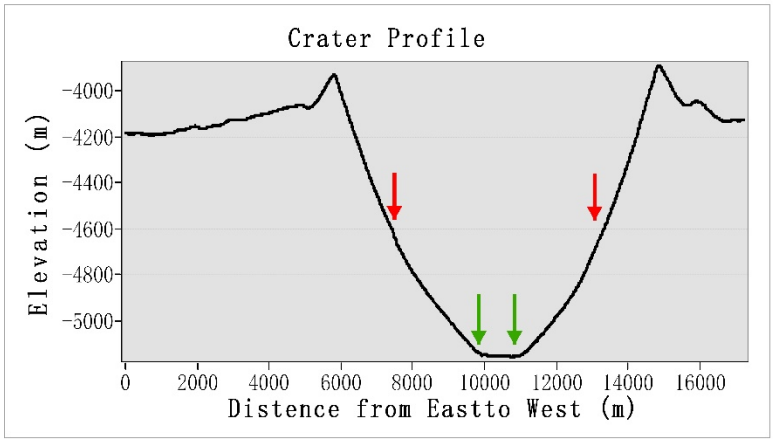

a

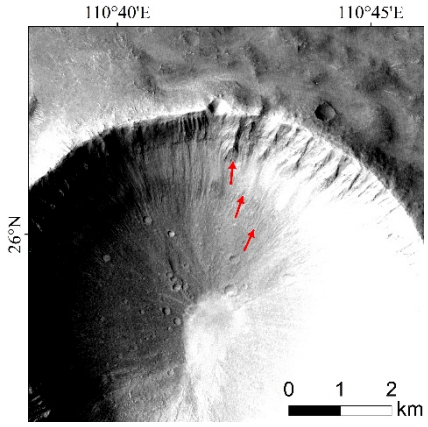

b

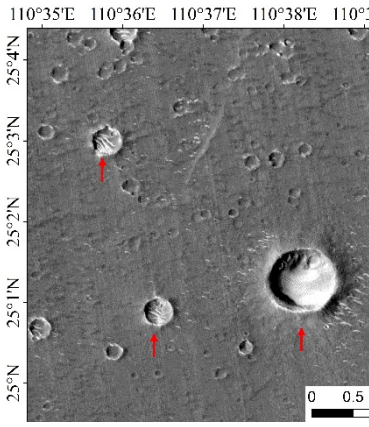

c

Figure 5 (a) Flat bottom crater and pit wall stratum outcrop; (b) Pit wall formation outcrop (CTX mosaic ID: E108_N24); (c) There are obvious dunes at the bottom of craters buried by aeolian sand.

We realized the stratigraphic interpretation of the Zhurong landing site by constructing a three-dimensional strata model. Accurate measurement of the formation structure requires a DEM with high accuracy. However, the resolution of the existing global DEM: MEX HRSC MOLA blended DEM is only 200 m, which cannot meet the needs of formation depth measurement. Hence, with the help of Integrated Software for Imagers and Spectrometers (ISIS3) and Ames Stereo Pipeline (ASP), we used CTX image and stereo image matching method to make the CTX DEM of the Zhurong landing site (Figure 6 (a)). The resolution of CTX DEM is 8m/pixel. However, due to the limitation of CTX image overlap, the final DEM will have missing data in many places. Therefore, when measuring the stratum, we only obtain the depth relative to the surface, rather than the absolute elevation overlap and use the HiRIC DEM to supplement the stratum measurement data where CTX DEM data are missing (Figure 6 (b)).

The MEX HRSC MOLA blended DEM shows that the terrain of the Zhurong landing site is very flat, so it is feasible for us to use planes to simulate the surface of the Zhurong landing site and determine the depth of each stratum. Although DEM products provided by HiRIC (60 km×150 km) cover only the eastern half of the three-dimensional stratum model, they still provide us with a method to test the reliability of stratum depth measurements. After comparison, we find that the difference between the formation depth measured by the CTX DEM and that measured by the HiRIC DEM is less than 10 m, which is less than 1% of the thickness of the VB group (Buczkowski et al., 2004) and has no impact on the formation interpretation results. It is shown that the method of measuring formation depth by a high-resolution DEM is reliable.

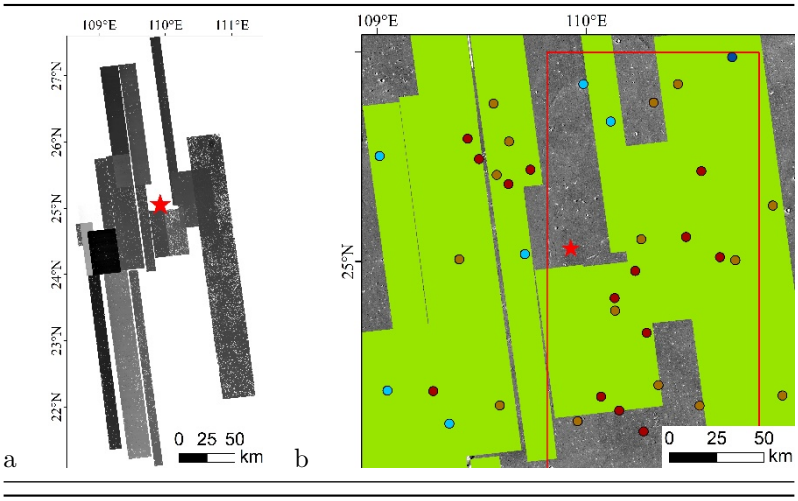

Figure 6 (a) DEM generated by CTX stereo images, (b) comparison of high-resolution DEM coverage area, red: HiRIC DEM coverage, green: CTX stereo relative DEM coverage, blue points: crater of the first layer for stratum mea-

surement, broun points: crater of the second layer for stratum measurement, red points: crater of the third layer for stratum measurement. Some craters are located outside the CTX DEM and measured by the HiRIC DEM.

When comparing strata, we comprehensively consider the statistical law, crater morphology and regional tectonic background. According to the regional tectonic background, there is no large-scale compression and tensile structure and no trace of magmatic erosion at the Zhurong landing site, so the strata in this area are distributed horizontally. The measurement results belong to which stratum are determined by the morphology of craters. Craters are classified into four types: (1) The crater is surrounded by a large number of rocks (Figure 7(a) red arrow) or secondary craters (Figure 7(a) yellow arrow), but corrugated ejecta cannot be formed. Such a crater is formed in a dry environment lacking volatiles. Thus, the stratum corresponding to these craters is named dry sedimentary strata section. (2) Around the crater is corrugated ejecta (Figure 7(b)) which represents a wet environment with a few volatiles. The stratum corresponding to these craters is named wet sedimentary section; (3) The crater has a significantly deeper depth than type 1 and 2 craters and is surrounded by a rampart (Figure 7(c)) which indicates a rich volatiles environment. The stratum corresponding to these craters is named VB section. (5) In addition, some craters are shallow and not surrounded by rocks, secondary craters, corrugated ejecta and rampart. These craters may correspond to the ejecta block (Figure 7(d)).

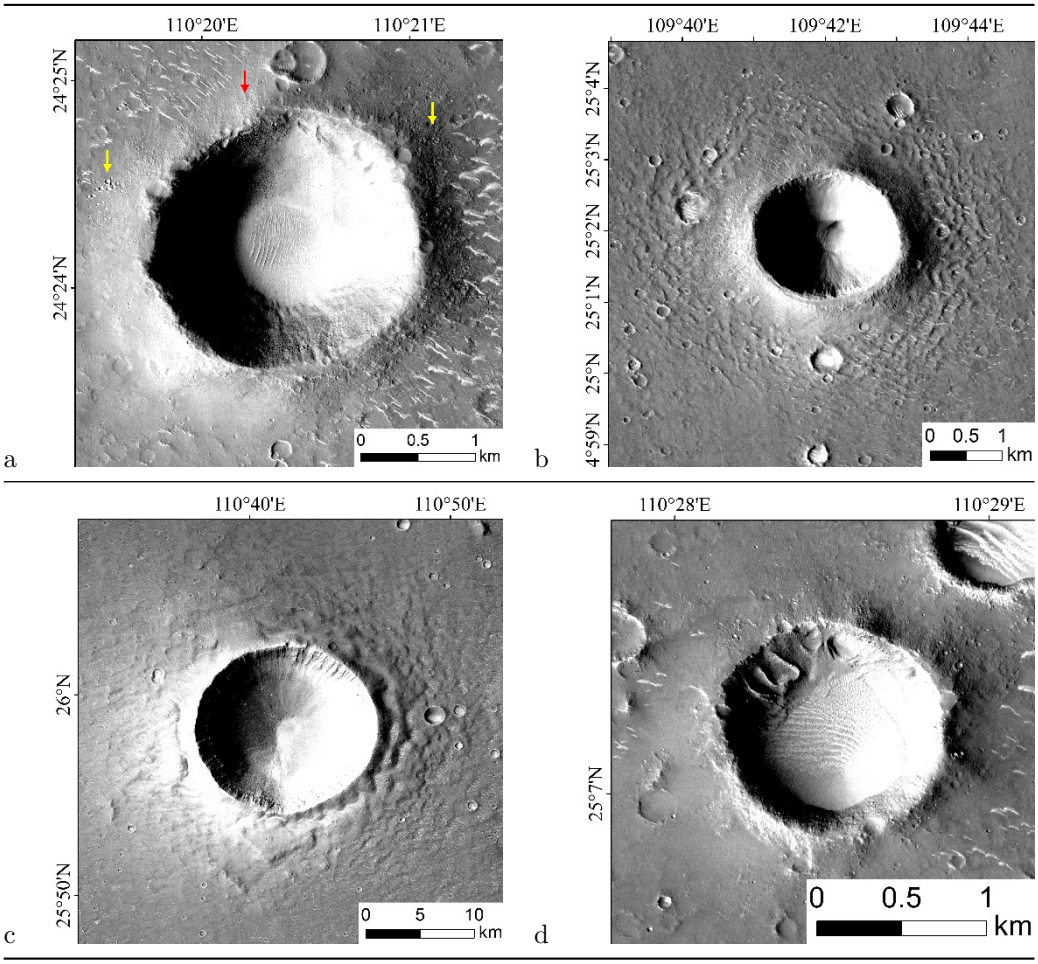

Figure 7 (a) Crater corresponding to the dry sedimentary section: It is dry outside the crater, with rocks (red arrow), secondary craters (yellow arrow); (b) Crater corresponding to the wet sedimentary section: the corrugated ejecta formed outside the crater (CTX mosaic ID: E108_N24); (c) Crater corresponding to the VB section: forming rampart (CTX mosaic ID: E108_N24); (d) Ejecta layer crater: It is dry and without rock and secondary craters.

3.3 Spectral observation

For CRISM spectral data, we use the analysis toolbox CAT to perform photometric correction, volcano scan atmospheric correction, removing strip and other preprocessing steps on the raw radiance to obtain the Mars surface reflection spectrum I/F (Seelos, 2009). For the orbit spectrum data of MMS, spectral radiance on the sensor is divided by pi times solar spectral irradiance (Bakker et

al., 2014; Fox et al., 2016). Then, convert it from radiance to surface reflectance in order to unify it into the I/F standard of CRISM. Removing the continuum on the source spectrum can obtain a spectral curve with enhanced absorption characteristics, which is helpful for the identification of material components (Kruse, 1994). In the experiment, we first locate all the high points on the spectrum, and combine the line segments that connect every two adjacent high points without crossing the spectrum to obtain a continnum Next, divide the source spectrum by the extracted continuum to remove the continuum (Wei, 2017). Finally, both CRISM and MMS spectral data are used to check whether the material of all the cones near the landing point is consistent. CRISM would be used to detect the mineral composition of cone because it has a wider spectral range.

We selected 16 cons around Zhurong landing points are in the spectral experiment (Figure 8(a)). No. 1 located in CRISM frt 000235c3_07_ra166 and MMS. NO. 2-13 located in CRISM msv 0003184e_01_ra152s. NO. 14-16 only located in MMS. Thus, Cones No. 2-16 are used to check whether the material of all the cones near the landing point are the same. Cone No. 1 (Figure 8(b)) is used to check whether the results of all the three images are consistent and get the the mineral composition of cone.

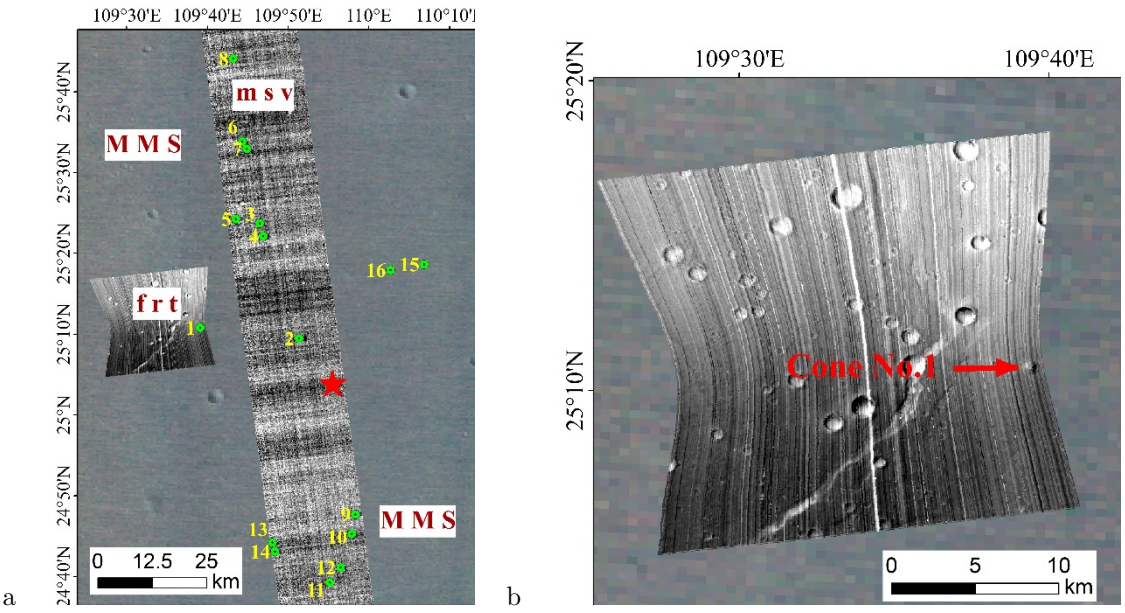

Figure 8 (a) Position of CRISM frt, msv and Tianwen-1 MMS, green points cones observed by spectral data; (b) Position of Cone No. 1 on Crism frt.

3.4 Analysis of crustal thickness and magnetic field anomalies

The anomaly of the planetary gravity field is caused by the fluctuation of the surface shape of its star and the spatial anomaly distribution of the internal material density. The planetary crustal thickness can be retrieved by combining gravity data with topography. The crustal thickness reflects the transformation of the crustal layer by magmatic activity (Wieczorek, 2004). The thickness of the crust is affected by a variety of geological processes, such as meteorite impact and mantle uplift, which will lead to the thinning of the crust, while the crust will be thickened after the magma from volcanic eruption solidifies. The analysis of the distribution characteristics of crustal thickness can help to find the deep dynamic process causing the change in surface morphology.

In the study of the internal structure and formation of planets, the magnetic field is also one of the important physical fields to study planets. Martian remanence is closely related to the Martian geological structure and internal dynamic process. After the shutdown of the Martian generator, large-scale magmatic activity will cause the magnetic body to be heated and demagnetized, so the magnetic field intensity is low in the younger igneous rocks on Mars (Mittelholz, 2020). In addition, large-scale crater events damage the upper crust containing strongly magnetized materials, resulting in the weakening of magnetic field intensity in some areas (Gong, 2021). Due to the low resolution (0.25°/pixel) of the magnetic field intensity image on the surface of Mars, the isoline of the magnetic field intensity is extracted in the experiment to find the magnetic anomaly.

It Is difficult to judge the origin of single crustal thickness and magnetic anomaly. Therefore, combined with previous research results (Wieczorek, 2004; Mittelholz, 2020; Gong, 2021), we observe whether there is a magnetic field intensity anomaly at the location of the crustal thickness anomaly found and observe the following morphological characteristics: (1) the gravity and magnetic anomaly caused by the meteorite impact is judged by the area covered by a large crater with thin crust and weak magnetic field intensity; (2) if the crust is thickened and the area with a magnetic anomaly is covered by volcano or lava, it is recognized as volcanic activity; and (3) if the crust is thickened and there is a magnetic anomaly, and there are no obvious characteristics such as volcanic activity on the surface, it is recognized as magma chamber activity in the deep crust. For the latter two cases, the enhancement of the magnetic anomaly indicates that the magmatic activity was at the same time or earlier than the Martian engine; otherwise, it indicates that the magmatic activity was after the Martian engine stopped.

4. Results

4.1 Results of Morphology and gravity/magnetic inversion

There are several explanations for the cone shapes where Zhurong landed, including mud volcano effects, volcano effects, hydrovolcanic origin, etc. (Wu et

al., 2021). We collected 592 cone shapes from the HiRIC images and found that they were of low strength. As shown in Figure 9(a), the craters left on the cone by aerolites are larger in diameter. These craters have simpler structures without concentric cycle shapes in Figure 9(b). According to the experiments by Kawakami, etc. (1983) and Miautani, etc. (1983), we believe these cones are composed of loose mud rock with lower intensity instead of basalt with high intensity (Figure 9(b)). In addition, some cones are found in the form of lobate and flow-like features (Figure. 9(c)(d)), which also shows that the cones are from mud volcanoes rather than lava volcanoes. A study from Ivanov, etc. (Ivanov, 2014) shows that mud upwelled beneath the Utopia Planitia, spewing out from weak spots to form erosion streams and cones. Cones in Zhurong landing site are less likely to be pingos. They have smooth surfaces and no cracks or fissures, which are supposed to be the typical characteristics of pingos (Depablo, 2009).

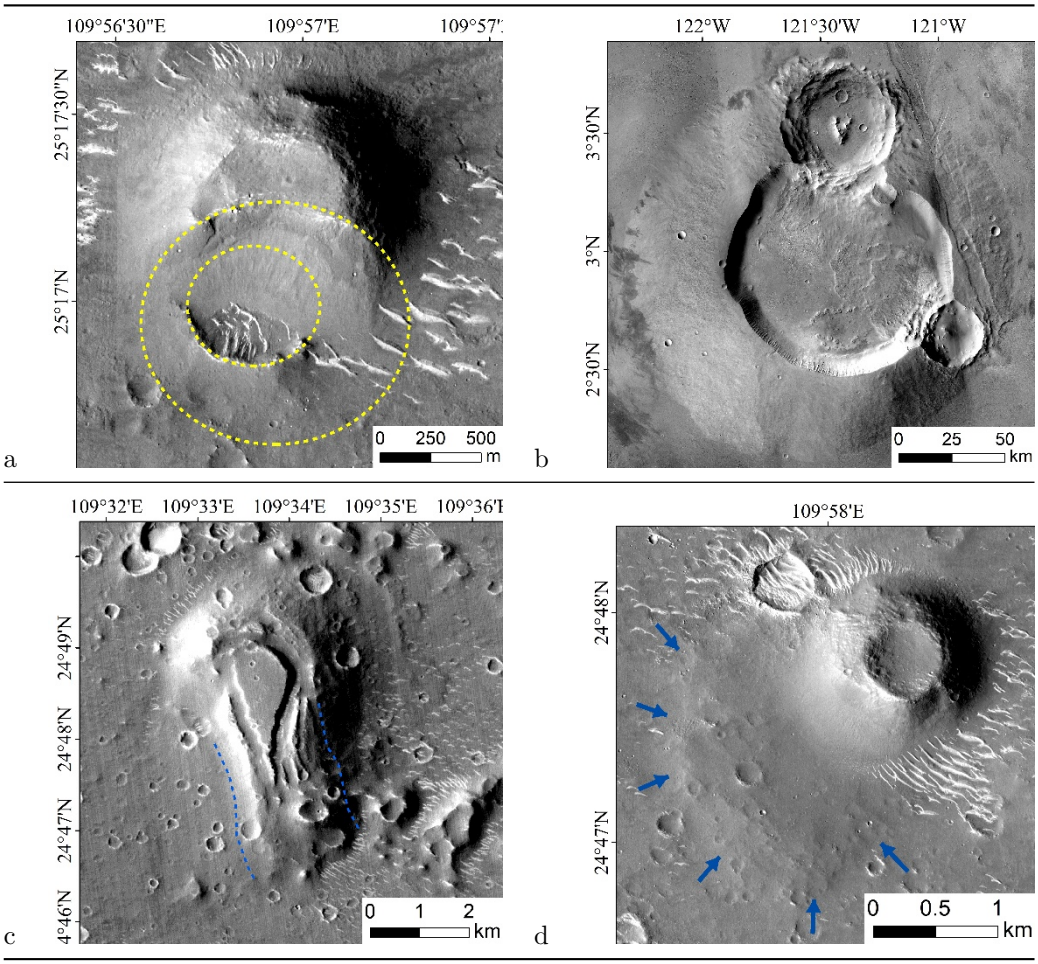

Figure 9. (a) Impacted mud volcano, (b) impacted basalt volcano with concentric circle structure in crater (CTX mosaic ID: E-124_N00), (c) flow-like features associated with cone, (d) lobate features associated with cone.

We measured the diameter and height of 295 cones using HiRIC DEM. The base width of cones varies from 45 m to 1127 m, with an average size of 346 m. The heights range from 2 to 84 m with a mean value of 27 m. With the help of HiRIC DEM, height/diameter data for the pitted cones in this area can be measured on a high-resolution DEM and can be clearly divided into toe parts (mud volcano and rootless cone). These cones are also similar in scale to other putative mud volcanoes and rootless cone on Mars (Figure 10). The height and basal diameter ratios of scoria/cinder cones as well as tuff rings/cones are larger than the cone features measured in our study. The comparison of the morphology of the pitted cones supports the mud volcano and rootless cones origin hypothesis.

[CHART]

Figure 10. Morphometric comparison between the cones measured by this study and previous.

The coverage of the ejecta block can be identified by the edge of the steep cliffs with the help of DEM and imaging. The HiRIC image carried by Tianwen-1 can offer a high-resolution DEM to effectively divide ejecta areas. (Figure 9, as a result mud volcanoes statistics and ejecta division can only be carried out within the coverage of the HiRIC image). On this basis, we calculated the number of mud volcanoes per square kilometer in different areas (Table 3). The results show that mud volcanoes density can reflect ejecta coverage. In areas without ejecta coverage, the number of cones per square kilometer was less than 0.03 (Table 3, blocks a, d, f), and in the area with ejecta coverage, the number was more than 0.03 and even over 0.1 as the amount of ejecta increased (Table 3, blocks c, e, g).

Table 3: Mud volcanoes data statistics in different blocks

Blocks	Type	Mud volcanoes quantity	Area/km^2	Mud volcanoes density/km^{-2}
a	original surface	3	2248.22	0.001334
b	ghost crater ejecta	0	30.11	0
c	ejecta	98	2850.93	0.034381
d	original surface	16	786.85	0.020334
e	ejecta	1	6.03	0.165729
f	original surface	1	97.94	0.010267
g	ejecta	115	2975.82	0.038645

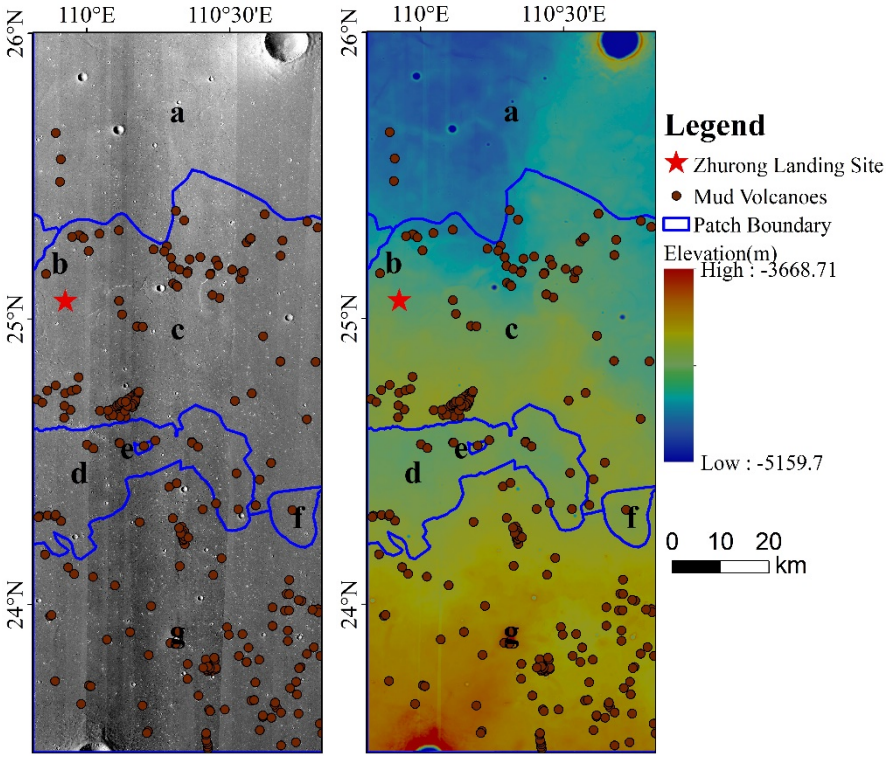

Figure 11. Ejecta blocks division and mud volcanoes distribution map. Base map: HiRIC panchromatic images and DEM, Brown points: mud volcanoes, Blue line: Block boundary.

As shown in Figure 12(a), the crustal thickness map shows a red area with thick crust in the southeast, which overlaps with the 50 nT isoline coverage area in the southeast. Many cones and mesas (Figure. 12(b)) can be seen in the CTX image. We infer that deep magmatic activity has resulted in crustal thickening and weak magnetic anomalies. Mittelholz (2020) believed that the dynamo of 4.5~3.7 Ga activity caused magnetization of the Mars crust. In reference to his opinion, we think that the weak magnetism in this region formed in the Utopia Planitia and was caused by the heating of deep magmatic activity after the Mars dynamo was stopped.

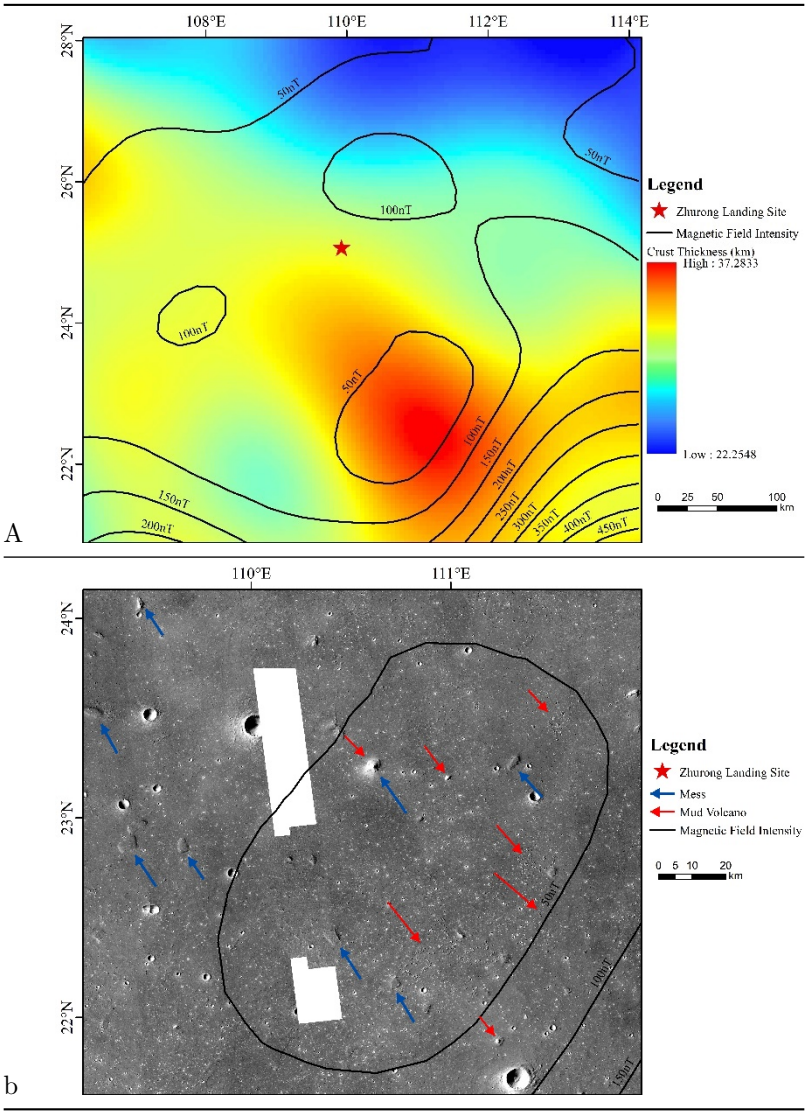

Figure. 12. (a) Crustal thickness and magnetic field intensity of the Zhurong landing site, base map: crustal thickness of the landing site, isoline: magnetic field intensity of the landing site; (b) Geomorphic map of gravity and magnetic anomaly area, blue arrow: mesas; red arrow: mud volcano (CTX mosaic ID: E108_N20, E108_N24).

4.2 Result of spectral

Cone No. 1 is in diameter and in height and belongs to a mud volcano. The spectral result in Figure 13(a) suggests MMS and CRISM give similar spectral

curves. In addition, the hypothesis that the composition of mud volcanoes in the landing area of Zhurong is consistent is verified for cones No. 2-16 show almost the same spectral curves (Figure 13(b)(c)). Spectral curves of cone No. 1 represents mud volcanoes may contain iron oxide minerals, such as hematite (absorption characteristics near 0.53 m), carbonate minerals like tharandite (absorption characteristics near 3.0 m), layered silicate mineral like palagonite (absorption characteristics near 2.0 m and 3.0 m) (Figure 13(d)). The formation of all the above minerals requires a wet environment with water. What's more, by comparing the CRISM spectral curve of No. 1 cone with the olivine C1PO77 in CRISM standard spectral library at 1 m, we can indicate that the cones in Zhurong landing site do not contain olivine. The result of spectral also prove that these cones are mud volcanoes.

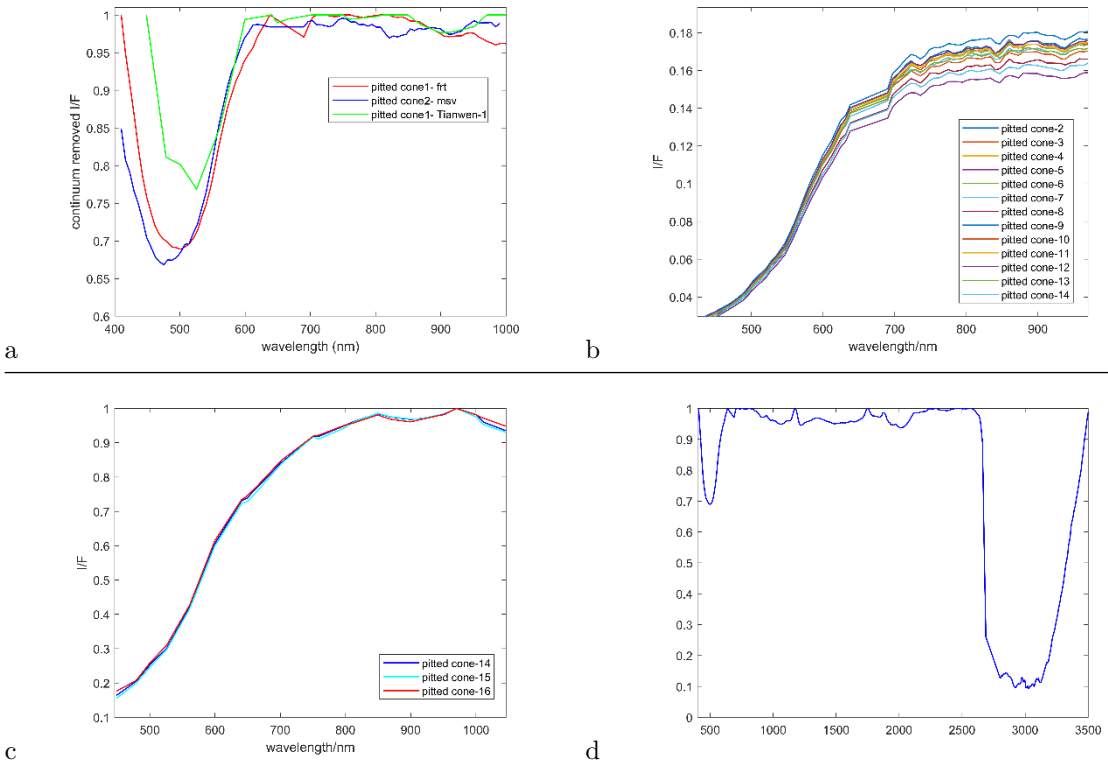

Figure. 13. (a) Spectral cuves of cones No. 1 from CRISM frt, msv, Tianwen-1 MMS; (b) Spectral cuves of cones No. 2-14 from CRISM msv; (c) Spectral cuves of cones No. 14-16 from Tianwen-1 MMS; (d) Complete spectral cuves of cones No. 1 from CRISM frt.

4.3 CSFD dating results

The existing geological map shows that the Zhurong landing site was formed in the Late Hesperian, which may have experienced a complex evolutionary history such as the Noachian impact, volcanic lava filling in the Early Hesperian, and ancient lakes forming and disappearing in the Late Hesperian Period (Wu et al., 2021). In our study, 14,000 craters (with diameters greater than 200 m, Figure 14(a)) were extracted within 200×200 km for dating. The dates of the different events were fitted by a differential fit using the Craterstats 2.0 tool, with the lunar chronology function (CF) and the production function (PF) from Ivanov et al. (2001). The dating results were 1.66 Ga, 3.43 Ga and 3.66 Ga (Figure. 14(b)), which were consistent with earlier studies (Wu et al., 2021). The dating results show that the VB unit of the Zhurong landing site surface was formed at approximately 3.43 Ga, and the formation of Utopia Planitia occurred earlier than 3.66. The younger age estimate (1.66 Ga) perhaps reflects the later resurfacing events, the nature of which is not clear.

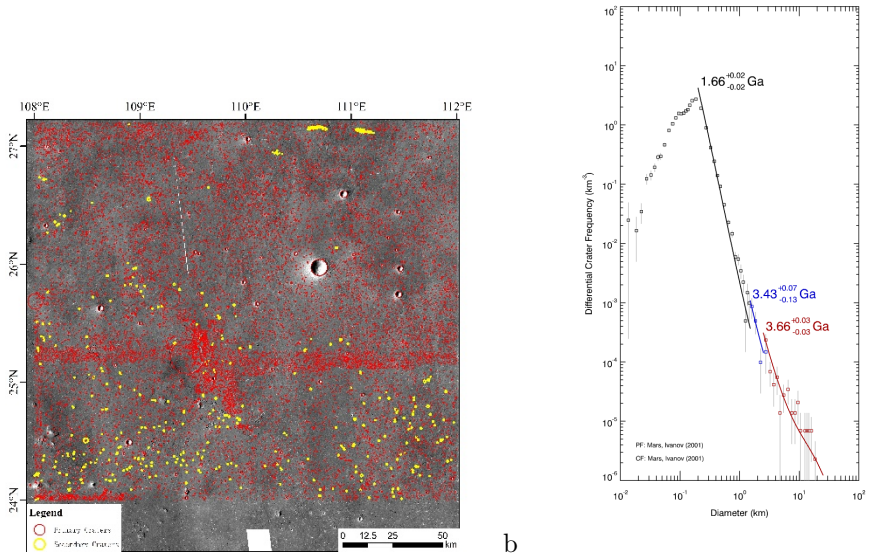

A b

Figure 14. (a) Schematic diagram of crater extraction, red circles: primary craters, yellow circles: secondary craters(CTX mosaic ID: E104_N20, E104_N24, E108_N20, E108_N24, E112_N20, E112_N24), (b) dating image of the Zhurong landing site.

4.4 The 3D strata model

Since flat-bottomed craters reflect the boundary between different strata, we selected 37 flat-bottomed craters within the 2°×2° range around the Zhurong landing site (serious craters have been filled with removed sand, and some deep craters expose two strata) with diameters ranging from 490 m to 8.3 km. The CTX DEM and HiRIC DEM were used to measure the depth of the strata at the landing site. Figure 15(a) shows the measured depth of the selected flat-bottled crater and the stratum protruding point. The strata identified by craters in the Zhurong landing site are VB in the Late Hesperian. The first stratum is in a dry sedimentary rock segment, and there are 15 craters exposing the first stratum, which are evenly distributed at the landing site. When at depths of 250 m, the craters has corrugated ejecta outside (Figure. 6(b)), indicating that the second layer has a high water content, which is consistent with the formation background of the VB material. Therefore, we infer that the formation is a humid sedimentary rock segment. The boundary between strata 2 and 3 was measured not only in the smaller flat-bottomed crater but also in the crater wall 68 km northeast of the landing site (red circle in Figure. 15(b)). Seven craters expose the second stratum, most of which are in the western half of the study area. The third stratum is deep and only appears in the bottom center of the crater in Figure 15(b) (also the crater in Figure 7(c)). Because the bottom of the larger crater is often filled, the third stratum cannot be observed. Only the barrier of the large crater indicates that this layer contains plenty of water/ice and belongs to the VB segment. The measured depths of the three strata from the flat-bottomed craters are as follows: the first stratum extends from the surface to a depth of 90-210 m underground, the second extends to a depth of 250-360 m and the third extends to 900 m underground, which is the deepest stratum identified in this experiment. In addition, a large number of cones, similar in shape and size to mud volcanoes on Earth, are present in the area, indicating intense hydrothermal activity in the past. The topographic features also indicate much ejecta scattered over the surface. After measurement, the ejecta has 23 corresponding craters, which are between 15 and 100 meters thick and can cover more than 60 percent of the landing site surface.

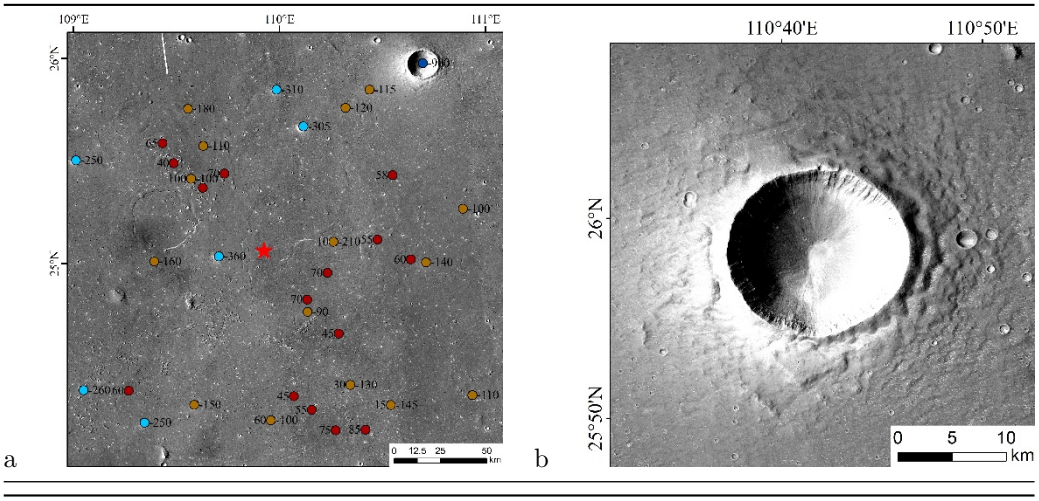

Figure 15. (a) Strata measurement points of the Zhurong landing site, red: ejecta stratum, brown: first stratum, light blue: second stratum, dark blue: third stratum (CTX mosaic ID: E108_N24); (b) boundary outcrops of strata 2 and 3 on crater walls (base map: CTX mosaic E108_N24, HiRIC panchromatic images).

Based on the formation measurement results obtained, we further developed a 3D formation model (Figure 16). First, the measurement points in the same stratum are selected, and an irregular triangular network (TIN) is made to form the model of the ejecta block and the interface of each stratum. Blocks are then fabricated within the range of adjacent TINs to form a model of the stratigraphic structure. According to the material composition of each stratum, the appropriate symbol texture filling blocks are selected, and the three-dimensional stratum model that reflects the stratum burial, depth and thickness, occurrence and rock properties is finally made.

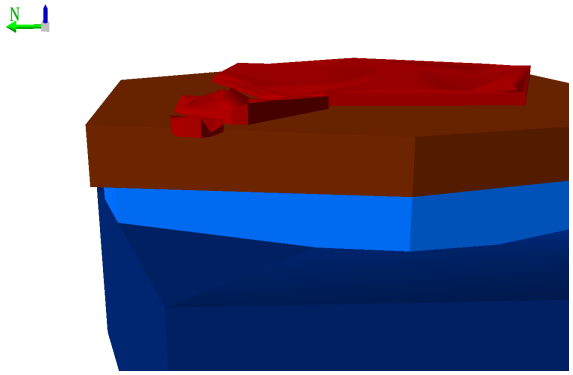

Figure 16. 3D strata model of the Zhurong landing site: red: ejecta block;

brown: dry sedimentary rock; light blue: wet sedimentary rock; dark blue: VB.

In the 3D strata model, the brown stratum represents the first stratum, which is a dry sedimentary rock segment located 90-210 m down the surface. The wet light blue stratum represents the second stratum, which is a section of wet sedimentary rock. It is 250-360 m below the dry sedimentary stratum, which had plenty of water interaction in the past. The third stratum is shown in dark blue as the VB segment. All three strata are composed of VB material. In addition, there are patches of ejecta in the first formation (shown in red in the 3D formation model). The 3D strata model shows that the wet sedimentary rock layer gradually thickens from south to north, which is consistent with the trend of VB gradually thickening from periphery to center in the whole Utopia Planitia (Buczkowski, 2004), indicating that our 3D strata model can accurately reflect the underground structure.

Analysis

5.1 Structure of the Strata

The 3D strata model shows that the VB thickness of the Zhurong's landing site is over 900 m. Some researchers have studied the aquifer of the Zhurong landing site. The results of Wu et al. (2021) show that the minimum VB thickness in this region is 65.5-268.3 m. They believe that VB is greater than the height of the buried crater rim and therefore use the relationship between the edge height of the fresh crater and the diameter of the crater (Garvin, 2003) to estimate the edge height of the ghost crater as the VB thickness. These two vastly different results are due to different interpretations of ghost craters. We believe that it is far from sufficient to estimate the VB thickness by burying the crater edge alone, which would result in the wall of the ghost crater being exposed after volume compaction like Figure 17(b). Such case obviously did not occur at the ghost crater in the Zhurong landing site. In addition, when the crater is deeper than 250 m, the content of volatile components reflected in the sputtering mat morphology also gradually increases (Figure 17(c-e)). Such case also indicates that the rich volatiles VBs should be thicker than 250m to cause the ejecta transformation as craters go larger.

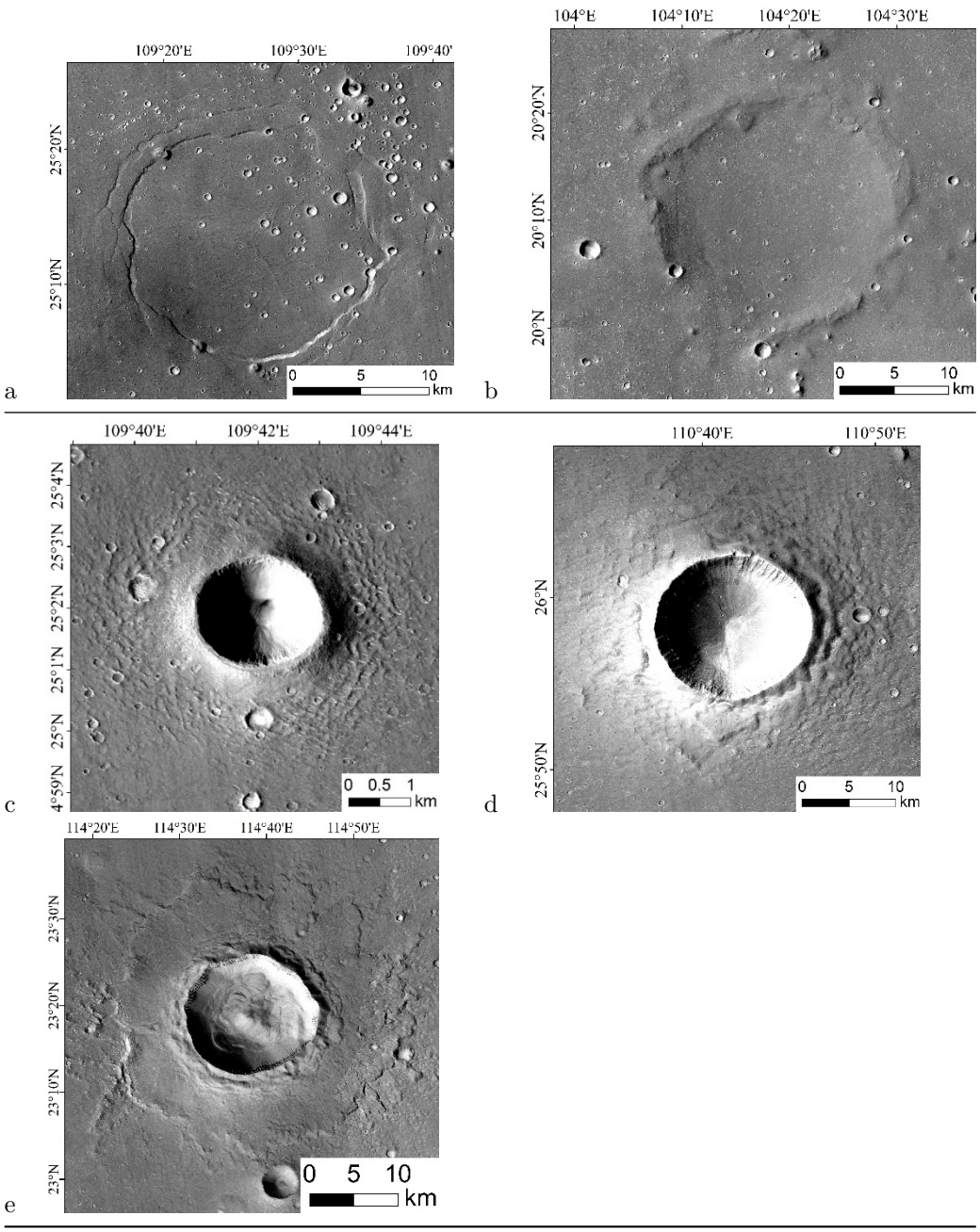

Figure 17. (a) ghost crater in Zhurong landing site; (b)nearly buried crater which is 439km south-west to the Zhurong landing site; (c) 1.8 km in diameter, 360 m in depth (CTX mosaic ID: E108_N24); (d) 8 km in diameter, 900 m in

depth (CTX mosaic ID: E108_N24); (e) 14 km in diameter and 860 m in depth, filled by upwelling mud (CTX mosaic ID: E112_N20).

In summary, we believe that the thickness of the VB group at the Zhurong landing site is 1.2 km. As the Martian climate changed from humid to dry, the difference in the water loss rate of VB at various depths resulted in the consolidation and diagenesis of VB materials in distinct periods and finally formed the three-strata structure in the three-dimensional geological structure.

5.2 Confirmation and genesis of mud volcanoes

Oehler et al. (2010) analyzed the cone of the Acidalia Planitia and judged it as a mud volcano. However, Wu et al. (2021) believe that the cone in the landing area of Zhurong does not have similar flow characteristics to mud volcanoes in the Asidalia Plain. After studying the cone in the Hephaestus Fossae area, 823 km southeast of the Zhurong landing site, Dapremont (2021) and others believe that it lacks fluidity, and the near-infrared spectrum at the edge of the vertebral body has the characteristics of olivine, which is considered to be the product of igneous rock. In addition, Soare et al. (2005, 2013, 2020) and Depablo et al. (2009) proposed the possibility of pingos. Ye et al. (2021) use HiRISE images and CTX DEMs to determine whether the cones are mud volcanoes. With the help of HiRIC and THEMIS Huang et al. (2020) are also more inclined to interprete the cones as mud volcanoes.

In fact, Oehler et al. (2010) pointed out that the morphology of mud volcanoes is diverse, which is also consistent with the conditions at the Zhurong landing site. In addition, from the pictures provided by Wu et al. (2021), it seems that they focus on the clustered cone, ignoring the fluidity phenomenon shown in Figure 9 (cd) of this paper. Although supported the mud volcano origin hypothesis of the cones, Huang et al. (2022) still leave the possibility of some igneous volcanic origin. They pointed out that the relatively low TI values (unit of J m^{-2} K^{-1} $s^{-1/2}$) materials may be interpreted as not only mud (fine-grained sediments), but also unconsolidated carapace of ash or volcanic ash deposits. What's more, it is hard to accurately assess the inconsistency between the cones and the other features due to gravity, atmospheric conditions, erosion rates and so on. Thus, spectral data from CRISM and MMS are important in the study of cones. They perform better in resolution and can directly indicate the composition of cones. Different with Dapremont (2021), our work does not find the absorption characteristics of olivine at 1.0 m. We find the absorption characteristics of hematite, tharandite and palagonite. Such mineral assemblage suggests water bearing mud volcanism rather than dry lava volcanism. Morphometry results of height and diameter of cones suggest some smallest cones are likely to be rootless cones. However, limited by the resolution of HiRIC DEM, this inference needs further confirmation. Anyhow, work of Depablo et al. (2009) still has a high reference value for mud volcanoes because, like pingos, mud volcanoes and rootless cones also need enough heat to melt the buried ice.

Rodriguez et al. (2012) proposed that due to the pressurization of the aquifer, cracks were generated through the overlying cryosphere, and the fluid sediment mixture erupted through the pipeline composed of these cracks to form mud volcanoes. Soare et al. (2005, 2013, 2020) believed that the cone at the Zhurong landing site shows that the area has experienced intense hydrothermal activity. Ye et al. (2021) also indicate that there is a magma chamber to be the heat source for maintaining the mobility of the mud reservoir and groundwater system. However, there is no obvious magmatic erosion and not sufficiently deep crater in this area to reveal the structure below the VB formation. The spatial statistical, gravity and magnetic results provide clues for confirming the power source of mud volcanoes in this area. The statistical results show that the mud volcano density of the ejecta block at the Zhurong landing site increases significantly from north to south (Figure. 18 (a)), and traces of underground magmatism are revealed by gravity and magnetic observations in the southeastern Zhurong landing site. Combined with the distribution characteristics of mud volcanoes, we judge that the magmatism here provides energy for hydrothermal activities such as mud volcanoes. This also confirms the judgment of Depablo et al. (2009) and Ye et al. (2021) that there may be a heat source of magma chamber under the surface of Utopian basin (Figure. 18 (b)).

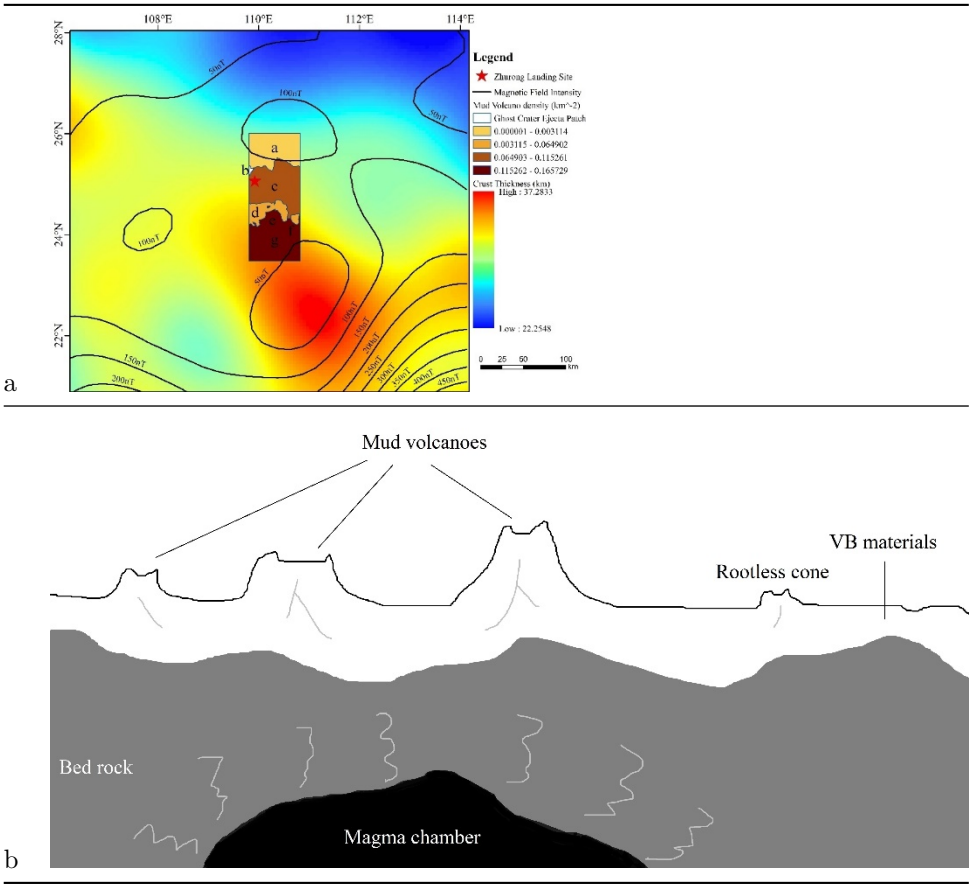

Figure 18(a) Density distribution, gravity and magnetic anomaly map of mud volcanoes; (b) Mud volcanoes genesis.

5.3 Influence of mud volcanism on ghost craters

There is a 19 km diameter ghost crater 30 km west of the Zhurong landing site. Such ghost craters are widely distributed in the southern Utopian Planitia. At present, its genesis includes differential compaction folds (Mcgill and Hills, 1992), the second graben formed by fold horizontal extension (Hobbs, 1967) and volumetric compaction (Buczkowski, 2004). Among them, the viewpoint of volume compaction considers the process of downward compaction of overburden materials along the inclined pit wall, which accurately explains the double ring graben of ghost crater. However, the inner graben of the ghost crater on the west side of the Zhurong landing site (Figure. 19 (a)) is much deeper than the outer graben, and the elevation within the inner graben is also significantly lower than that outside (approximately 80 m), showing stronger compaction. However, some ghost craters do not have such a significant internal and external elevation

difference (Figure. 159(b)). Therefore, the shape of the ghost crater on the west side of Zhurong may be dominated by more than the compaction caused by water evaporation. In cases where there are a vast number of mud volcanoes and ejecta blocks covering ghost craters, we calculated that the material loss of ghost craters was around 12.504 km^3 by subtracting the MEX HRSC MOLA blended DEM from the unreal 3D strata model which assuming that the ghost impact crater area is a plain . The volumes of the two muddy ejecta blocks are 1.244 km^3 and 10.940 km^3 obtained from real 3D strata model. The sum of them is close to the mass loss due to the ghost impacting force. This indicates that at places with drastic groundwater activity, such as Zhurong landing, in the process of forming ghost craters after the crater is buried by the VB, the upwelling and ejection of underground materials also plays a role in controlling the morphology of ghost craters.

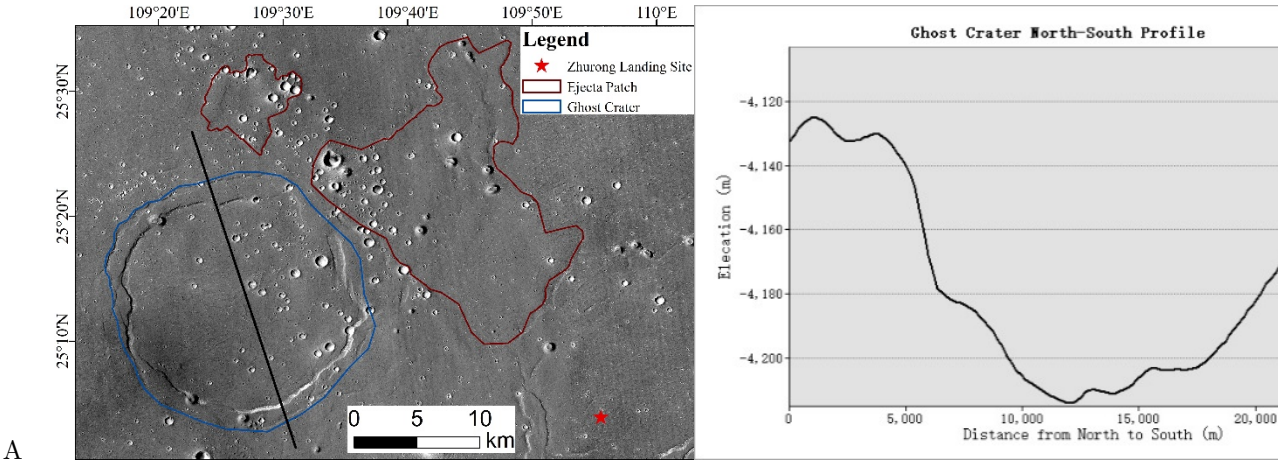

Figure 19(a) Ghost crater and topographic profile west of the landing site, blue: Ghost crater, red: ejecta block (CTX mosaic ID: E108_N24); (b) Ghost crater without material loss and its topographic profile (CTX mosaic ID: E104_N24, E108_N24).

Conclusion

We have derived more than 14000 craters at the Zhurong landing site and conducted geological dating. By taking advantage of the CTX image, we produced a DEM of the Zhurong landing site. By measuring 37 exposured strata due to craters on the CTX DEC and HiRIC DEM and combining the morphological features of craters and the structural background of the site, we produced a 3D strata model for the Zhurong landing site. Utilizing heavy magnetic data and morphological features, we have determined that the widely distributed cones on the Zhurong landing site are mainly mud volcanoes, other might be rootless cones. According to the distribution of mud volcanoes and topography, the distribution range of ejecta blocks is divided. Combining the 3D strata model and ejecta block distribution, we discussed the motion mechanism in the formation process of ghost craters.

The major conclusions are as follows:

1. The Zhurong landing site can be divided into 3 strata and ejecta blocks. The strata of the Zhurong landing site can be defined as dry sediment members, moist sediment members and VB members from the top to the bottom. The depth of VB group can amount to 1.2 km.

2) The morphological and spectral features show that the cones at the Zhurong landing site are mud volcanoes formed by groundwater activity. The heat source comes from the magma chamber located in the southern underground part. The density of the mud volcanoes can help determine whether the ejecta block exists. What's more, morphological features suggests that the smallest part of the cones might be rootless cones. The formation of ice, mud, and volcanism interaction in Zhurong landing site is diverse.

3) The 3D strata model of the Zhurong landing site indicates that apart from volume compaction, some ghost craters have extrusion of underground materials, resulting in the internal elevation being significantly lower than the external elevation

4 Currently, the Zhurong Rover is moving south; if it can arrive at the heavy magnetic abnormal area, the in situ detection data obtained are expected to provide more clues for possible underground magmatism and its transformation to the surface in this area. We look forward to more data returned by Zhurong Rover and Tianwen-1 in the future to further enrich the research on the geological evolution history of the landing inspection area.

Acknowledgements and Data

This work was supported by National Key Research and Development project (2019YFE0123300), Civil Aerospace Technology Pre-research Project of Na-

tional Defense Science and Industry Administration (No.D020103); Beijing Science and Technology Project (No.Z191100004319001).

The Tianwen-1 data used in this work is processed and produced by the Ground Research and Application System (GRAS) of China's Lunar and Planetary Exploration Program, provided by China National Space Administration (http://moon.bao.ac.cn). The HiRIC DEM, HiRIC panchromatic images and MMS data titles are listed in the following table, these data's acquisition are within protection period now, an account is needed to apply for them. But some of them can directly achieved at https://moon.bao.ac.cn/web/enmanager/zygj without account and application. The CTX mosaic images produced by the Malin Space Science Systems and Jet Propulsion Laboratory and panchromatic images are available at http://murray-lab.caltech.edu/CTX/tiles/beta01_tile-blended/. The MEX HRSC MOLA blended DEM is publicly available at https://astrogeology.usgs.gov/search/map/Mars/Topography/HRSC_MOLA_Blend/Mars_HRSC_MOLA_BlendDEM_Globa
Crustal thickness data and CRISM data can be obtained from NASA's Planetary Data System (PDS): https://ode.rsl.wustl.edu/mars/index.aspx

Table: HiRIC DEM and Tianwen-1 images titles

Titles	Directly achieved (T
HX1_GRAS_HIRIC_DEM_3.5_0000_244453N1101905E_A	T (equal to Mosaic
HX1_GRAS_HIRIC_DIM_0.7_0001_254537N1095850E_A	F
HX1_GRAS_HIRIC_DIM_0.7_0002_254537N1101905E_A	F
HX1_GRAS_HIRIC_DIM_0.7_0003_254537N1103919E_A	F
HX1_GRAS_HIRIC_DIM_0.7_0004_251515N1095850E_A	T
HX1_GRAS_HIRIC_DIM_0.7_0005_251515N1101905E_A	F
HX1_GRAS_HIRIC_DIM_0.7_0006_251515N1103919E_A	F
HX1_GRAS_HIRIC_DIM_0.7_0007_244453N1095850E_A	T
HX1_GRAS_HIRIC_DIM_0.7_0008_244453N1101905E_A	F
HX1_GRAS_HIRIC_DIM_0.7_0009_244453N1103919E_A	F
HX1_GRAS_HIRIC_DIM_0.7_0010_241431N1095850E_A	F
HX1_GRAS_HIRIC_DIM_0.7_0011_241431N1101905E_A	F
HX1_GRAS_HIRIC_DIM_0.7_0012_241431N1095850E_A	F
HX1_GRAS_HIRIC_DIM_0.7_0013_234409N1095850E_A	F
HX1_GRAS_HIRIC_DIM_0.7_0014_234409N1101905E_A	F
HX1_GRAS_HIRIC_DIM_0.7_0015_234409N1103919E_A	F
HX1-Or_GRAS_MMS-D-208-V_SCI_N_20220316031621_20220316034219_00989_A	F

Reference

Wan, W.X., Wang, C., Li, C.L. et al. China's first mission to Mars. Nat Astron 4, 721 (2020). https://doi.org/10.1038/s41550-020-1148-6

Depablo, M., & Komatsu, G. (2009). Possible pingo fields in the Utopia

basin, Mars: Geological and climatical implications. Icarus, 199(1), 49-74. Doi:10.1016/j.icarus.2008.09.007

Soare, R. J., Burr, D. M., & Wan Bun Tseung, J. M. (2005). Possible pingos and a periglacial landscape in northwest Utopia Planitia. Icarus, 174(2), 373-382. Doi:10.1016/j.icarus.2004.11.013

Soare, R. J., Conway, S. J., Pearce, G. D., Dohm, J. M., & Grindrod, P. M. (2013). Possible crater-based pingos, paleolakes and periglacial landscapes at the high latitudes of Utopia Planitia, Mars. Icarus, 225(2), 971-981. Doi:10.1016/j.icarus.2012.08.041

Soare, R. J., Conway, S. J., Williams, J. P., Gallagher, C., & Keown, L. E. M. (2020). Possible (closed system) pingo and ice-wedge/thermokarst complexes at the mid latitudes of Utopia Planitia, Mars. Icarus, 342. Doi:10.1016/j.icarus.2019.03.010

Ye, B., Qian, Y., Xiao, L., Michalski, J. R., Li, Y., Wu, B., & Qiao, L. (2021). Geomorphologic exploration targets at the Zhurong landing site in the southern Utopia Planitia of Mars. Earth and Planetary Science Letters, 576. https://doi.org/10.1016/j.epsl.2021.117199

Huang, H., Liu, J., Wang, X., Chen, Y., Zhang, Q., Liu, D., Yan, W., & Ren, X. (2022). The Analysis of Cones within the Tianwen-1 Landing Area. Remote Sensing, 14(11), 2590. https://www.mdpi.com/2072-4292/14/11/2590

Ivanov, M. A., Hiesinger, H., Erkeling, G., & Reiss, D. (2014). Mud volcanism and morphology of impact craters in Utopia Planitia on Mars: Evidence for the ancient ocean. Icarus, 228, 121-140. Doi:10.1016/j.icarus.2013.09.018

Mangold, N., Gupta, S., Gasnault, O., Dromart, G., Tarnas, J. D., Sholes, S. F., . . . Williford, K. H. Perseverance rover reveals an ancient delta-lake system and flood deposits at Jezero crater, Mars. Science, 0(0), eabl4051. Doi:doi:10.1126/science.abl4051

Wu, X., Liu, Y., Zhang, C., Wu, Y., Zhang, F., Du, J., . . . Zou, Y. (2021). Geological characteristics of China's Tianwen-1 landing site at Utopia Planitia, Mars. Icarus, 370. Doi:10.1016/j.icarus.2021.114657

McGill, G. E. (1989), Buried topography of Utopia, Mars: Persistence of a giant impact depression,Journal of Geophysical Research: Solid Earth (1978–2012),94(B3), 2753–2759.

Thomson, B. J., and Head, J. W. (2001), Utopia Basin, Mars: Characterization of topography and morphology and assessment of the origin and evolution of basin internal structure, J. Geophys. Res., 106(E10), 23209– 23230, doi:10.1029/2000JE001355..

Masursky, H., & Crabill, N. L. (1976). Search for the Viking 2 landing site. Science, 194(4260), 62-68.

Mills, M. M., McEwen, A. S., & Okubo, C. H. (2021). A Preliminary Regional Geomorphologic Map in Utopia Planitia of the Tianwen-1 Zhurong Landing Region. Geophysical Research Letters, 48(18). Doi:10.1029/2021gl094629

Tanaka, K. L., & Scott, D. H. (1987). Geologic map of the polar regions of Mars: US Geological Survey Miscellaneous Investigations Series. Map I-1802-C, scale: 1: 2,000,000.

Kreslavsky, M. A., and Head, J. W., Mars: Nature and evolution of young latitude-dependent water-ice-rich mantle, Geophys. Res. Lett., 29(15), doi:10.1029/2002GL015392, 2002.

Goossens, S., Sabaka, T. J., Genova, A., Mazarico, E., Nicholas, J. B., & Neumann, G. A. (2017). Evidence for a Low Bulk Crustal Density for Mars from Gravity and Topography. Geophys Res Lett, 44(15), 7686-7694. Doi:10.1002/2017GL074172

Langlais, B., Thébault, E., Houliez, A., Purucker, M. E., & Lillis, R. J. (2019). A new model of the crustal magnetic field of Mars using MGS and MAVEN. Journal of Geophysical Research: Planets, 124, 1542– 1569. https://doi.org/10.1029/2018JE005854

Dickson, J. L., Kerber, L. A., Fassett, C. I., & Ehlmann, B. L. (2018, March). A global, blended CTX mosaic of Mars with vectorized seam mapping: A new mosaicking pipeline using principles of non-destructive image editing. In Lunar and planetary science conference (Vol. 49, pp. 1-2).

Meng, Q., Wang, D., Wang, X., Li, W., Yang, X., Yan, D., . . . Dong, J. (2021). High Resolution Imaging Camera (HiRIC) on China's First Mars Exploration Tianwen-1 Mission. Space Science Reviews, 217(3), 42. Doi:10.1007/s11214-021-00823-w

McEwen, A. S., Eliason, E. M., Bergstrom, J. W., Bridges, N. T., Hansen, C. J., Delamere, W. A., . . . Weitz, C. M. (2007). Mars Reconnaissance Orbiter's High Resolution Imaging Science Experiment (HiRISE). Journal of Geophysical Research, 112(E5). Doi:10.1029/2005je002605

Malin, M. C., Bell, J. F., Cantor, B. A., Caplinger, M. A., Calvin, W. M., Clancy, R. T., . . . Wolff, M. J. (2007). Context Camera Investigation on board the Mars Reconnaissance Orbiter. Journal of Geophysical Research, 112(E5). Doi:10.1029/2006je002808

Fergason, R. L, Hare, T. M., & Laura, J. (2018). HRSC and MOLA Blended Digital Elevation Model at 200m v2. Astrogeology PDS Annex, U.S. Geological Survey. http://bit.ly/HRSC_MOLA_Blend_v0

Murchie, S., Arvidson, R., Bedini, P., Beisser, K., Bibring, J. P., Bishop, J., Boldt, J., Cavender, P., Choo, T., Clancy, R. T., Darlington, E. H., Des Marais, D., Espiritu, R., Fort, D., Green, R., Guinness, E., Hayes, J., Hash, C., Heffernan, K., . . . Wolff, M. (2007). Compact Reconnaissance Imaging Spec-

trometer for Mars (CRISM) on Mars Reconnaissance Orbiter (MRO). Journal of Geophysical Research, 112(E5).

He, Z., Xu, R., Li, C., Yuan, L., Liu, C., Lv, G., Jin, J., Xie, J., Kong, C., Li, F., Chen, X., Wang, R., Xu, S., Pan, W., Wu, J., Li, C., Wang, T., Jin, H., Chen, H., . . . Wang, J. (2021). Mars Mineralogical Spectrometer (MMS) on the Tianwen-1 Mission. Space Science Reviews, 217(2).

Barlow, N. G. (2006). Impact craters in the northern hemisphere of Mars: Layered ejecta and central pit characteristics. Meteoritics & Planetary Science, 41(10), 1425-1436. doi:https://doi.org/10.1111/j.1945-5100.2006.tb00427.x

Niu, S., Zhang, F., Di, K., Gou, S., & Bugiolacchi, R. (2021). Dating and Morphological Characterization of Layered Ejecta Craters in the Candidate Landing Areas of China's First Mars Mission (Tianwen-1). https://ui.adsabs.harvard.edu/abs/2021LPI....52.1786N

Dapremont, A. M., & Wray, J. J. (2021). Igneous or Mud Volcanism on Mars? The Case Study of Hephaestus Fossae. Journal of Geophysical Research: Planets, 126(2). doi:10.1029/2020je006390

Oberbeck, V. R., & Quaide, W. L. (1967). Estimated thickness of a fragmental surface layer of Oceanus Procellarum. Journal of Geophysical Research (1896-1977), 72(18), 4697-4704.

Ormö, J., Rossi, A. P., & Housen, K. R. (2013). A new method to determine the direction of impact: Asymmetry of concentric impact craters as observed in the field (Lockne), on Mars, in experiments, and simulations. Meteoritics & Planetary Science, 48(3), 403-419.

Senft, L. E., & Stewart, S. T. (2007). Modeling impact cratering in layered surfaces. Journal of Geophysical Research, 112(E11).

SENFT, L. E., & STEWART, S. T. (2008). Impact crater formation in icy layered terrains on Mars. Meteoritics & Planetary Science, 43(12), 1993-2013.

Herrick, R. R., & Hynek, B. M. (2017). Investigating target versus impactor influences on Martian crater morphology at the simple-complex transition. Meteoritics & Planetary Science, 52(8), 1722-1743.

Prieur, N. C., Rolf, T., Wünnemann, K., & Werner, S. C. (2018). Formation of Simple Impact Craters in Layered Targets: Implications for Lunar Crater Morphology and Regolith Thickness. Journal of Geophysical Research: Planets, 123(6), 1555-1578.

Martellato, E., Bramson, A. M., Cremonese, G., Lucchetti, A., Marzari, F., Massironi, M., Re, C., & Byrne, S. (2020). Martian Ice Revealed by Modeling of Simple Terraced Crater Formation. Journal of Geophysical Research: Planets, 125(10).

Plescia J. B. (2015). Transitional crater (simple/complex). In Encyclopedia of planetary landforms, edited by Hargitai H. and Kereszturi A. New York:

Springer. pp. 2173–2177.

Wilcox, B. B., Robinson, M. S., Thomas, P. C., & Hawke, B. R. (2005). Constraints on the depth and variability of the lunar regolith. Meteoritics & Planetary Science, 40(5), 695-710. doi:DOI 10.1111/j.1945-5100.2005.tb00974.x

Buczkowski, D. L., and Cooke, M. L. (2004), Formation of double-ring circular grabens due to volumetric compaction over buried impact craters: Implications for thickness and nature of cover material in Utopia Planitia, Mars, J. Geophys. Res., 109, E02006, doi:10.1029/2003JE002144.

Seelos, F. . (2009). CRISM Data Users ' Workshop Nili Fossae Data Processing Walkthrough.

Bakker, W. H., van Ruitenbeek, F. J. A., van der Werff, H. M. A., Zegers, T. E., Oosthoek, J. H. P., Marsh, S. H., & van der Meer, F. D. (2014). Processing OMEGA/Mars Express hyperspectral imagery from radiance-at-sensor to surface reflectance. Planetary and Space Science, 90, 1-9. doi:10.1016/j.pss.2013.11.007

Fox, V. K. , Arvidson, R. E. , Guinness, E. A. , Mclennan, S. M. , Catalano, J. G. , & Murchie, S. L. , et al. (2016). Smectite deposits in marathon valley, endeavour crater, mars, identified using crism hyperspectral reflectance data. Geophysical Research Letters, 43(10), 4885-4892.

Kruse, F., & Lefkoff, A. (1994). Knowledge-based geologic mapping with imaging spectrometers. Remote Sensing Reviews, 8(1-3), 3-28.

Wieczorek, M. A., and Zuber, M. T. (2004), Thickness of the Martian crust: Improved constraints from geoid-to-topography ratios, J. Geophys. Res., 109, E01009, doi:10.1029/2003JE002153.

Mittelholz, A., Johnson, C. L., Feinberg, J. M., Langlais, B., & Phillips, R. J. (2020). Timing of the martian dynamo: New constraints for a core field 4.5 and 3.7 Ga ago. Science Advances, 6(18), eaba0513. doi:doi:10.1126/sciadv.aba0513

Gong, S., & Wieczorek, M. (2021). Depth of Martian Magnetization From Localized Power Spectrum Analysis. Journal of Geophysical Research: Planets, 126(8). doi:10.1029/2020je006690

Kawakami, S.-I., Mizutani, H., Takagi, Y., Kato, M., & Kumazawa, M. (1983). Impact experiments on ice. Journal of Geophysical Research: Solid Earth, 88(B7), 5806-5814. doi:10.1029/JB088iB07p05806

Mizutani, H., Kawakami, S.-i., Takagi, Y., Kato, M., & Kumazawa, M. (1983). Cratering experiments in sands and a trial for general scaling law. Journal of Geophysical Research, 88(S02). doi:10.1029/JB088iS02p0A835

Ivanov, B. A., Neukum, G., & Wagner, R. (2001). Size-Frequency Distributions of Planetary Impact Craters and Asteroids. In M. Y. Marov & H. Rickman (Eds.), Collisional Processes in the Solar System (pp. 1-34). Springer Netherlands. https://doi.org/10.1007/978-94-010-0712-2_1

Hobbs, D. W. (1967), The formation of tension joints in sedimentary rocks: An explanation, Geol. Mag., 104, 550–556.

Garvin, J. B., Sakimoto, S. E. H., & Frawley, J. J. (2003, July 01, 2003). Craters on Mars: Global Geometric Properties from Gridded MOLA Topography.

Oehler, D. Z., & Allen, C. C. (2010). Evidence for pervasive mud volcanism in Acidalia Planitia, Mars. Icarus, 208(2), 636-657. doi:10.1016/j.icarus.2010.03.031